

AB-UPT: Scaling Neural CFD Surrogates for High-Fidelity Automotive Aerodynamics Simulations via Anchored-Branched Universal Physics Transformers

Benedikt Alkin^{*,1}, Maurits Bleeker^{*,1}, Richard Kurle^{*,1}, Tobias Kronlachner^{*,1}, Reinhard Sonnleitner¹, Matthias Dorfer¹, Johannes Brandstetter^{1,2}

^{*}Equal contribution

¹Emmi AI GmbH

²Ellis Unit, LIT AI Lab, JKU Linz

Correspondence to johannes@emmi.ai

Abstract

Recent advances in neural surrogate modeling offer the potential for transformative innovations in applications such as automotive aerodynamics. Yet, industrial-scale problems often involve volumetric meshes with cell counts reaching the 100 millions, presenting major scalability challenges. Complex geometries further complicate modeling through intricate surface-volume interactions, while quantities such as vorticity are highly nonlinear and must satisfy strict divergence-free constraints. To address these requirements, we introduce Anchored-Branched Universal Physics Transformers (AB-UPT) as a novel modeling scheme for building neural surrogates for computational fluid dynamics (CFD) simulations. AB-UPT is designed to: (i) decouple geometry encoding and prediction tasks via multi-branch operators; (ii) enable scalability to high-resolution outputs via neural simulation in a low-dimensional latent space, coupled with *anchored* neural field decoders to predict high-fidelity outputs; (iii) enforce physics consistency by a novel divergence-free formulation. We show that AB-UPT yields state-of-the-art predictive accuracy of surface and volume fields on automotive CFD simulations ranging from 33 thousand up to 150 million mesh cells. Furthermore, our anchored neural field architecture enables the enforcement of hard physical constraints on the physics predictions without degradation in performance, exemplified by modeling divergence-free vorticity fields. Notably, the proposed models can be trained on a single GPU in less than a day and predict industry-standard surface and volume fields within seconds. Additionally, we show that the flexible design of our method enables neural simulation from a computer-aided design geometry alone, omitting the need for costly CFD meshing procedures.

1 Introduction

Computational fluid dynamics (CFD) is central to automotive aerodynamics, offering in-depth analysis of entire flow fields and complementing wind tunnels by simulating open-road conditions. The fundamental basis of almost all CFD simulations are the Navier-Stokes (NS) equations, describing the motion of viscous fluid substances around objects. However, the computational cost of solving the NS equations necessitates modeling approximations, most notably regarding the onset and effects of turbulence. Therefore, CFD employs different turbulence modeling strategies, balancing accuracy and cost. In this context, seminal datasets, such as DrivAerNet (Elrefaei et al., 2024a;b) and DrivAerML (Ashton et al., 2024b) have been released, allowing for an in-depth study of deep learning surrogates for automotive aerodynamics. Especially, DrivAerML runs high-fidelity CFD simulations on 140 million volumetric cells with Hybrid RANS-LES (HRLES) (Spalart et al., 2006; Chaouat, 2017; Heinz, 2020; Ashton et al., 2022), which is the highest-fidelity CFD approach routinely deployed by the automotive industry (Hupertz et al., 2022; Ashton et al., 2024b).

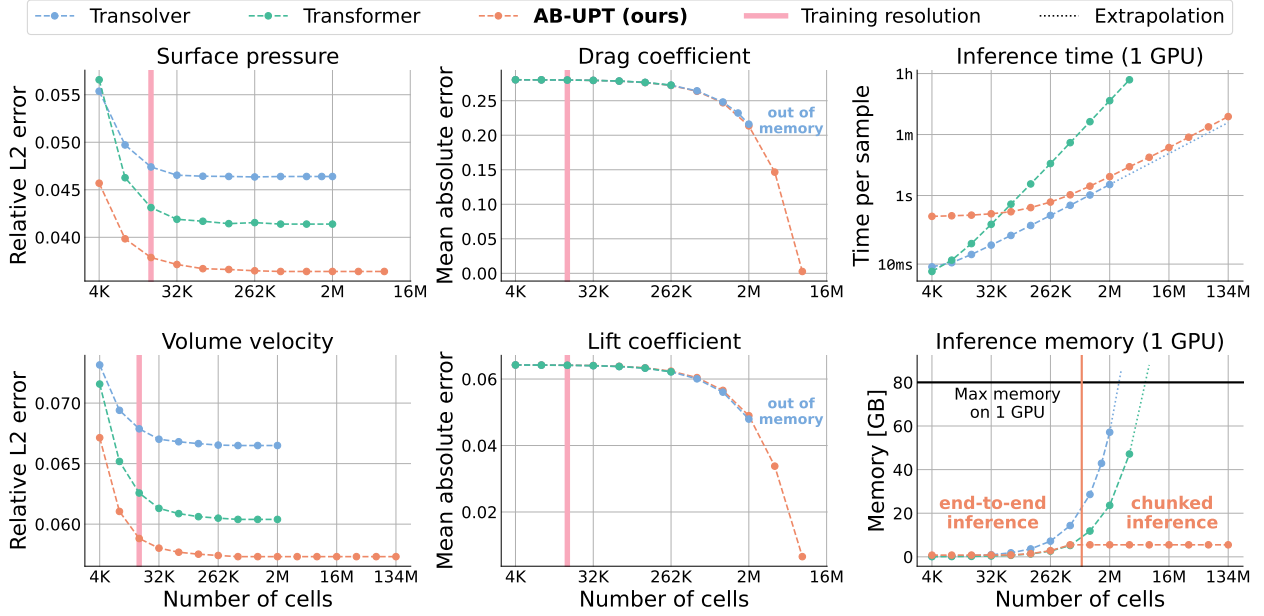
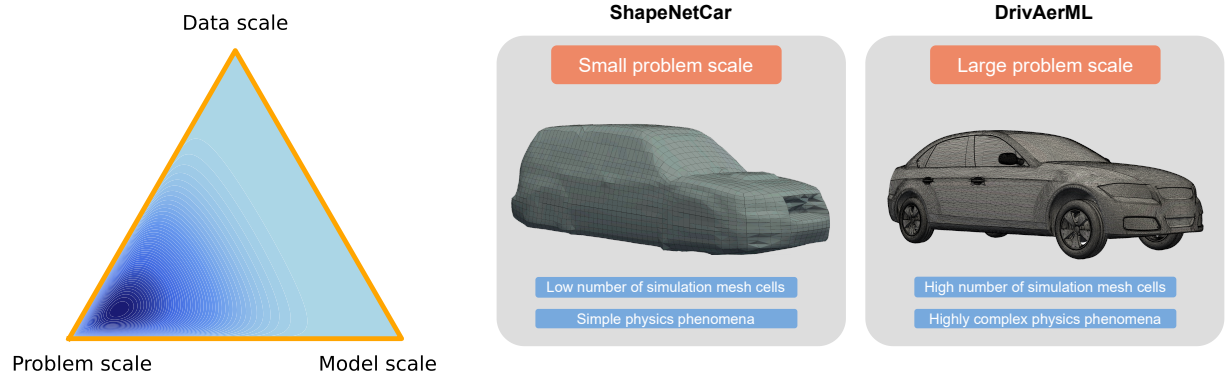
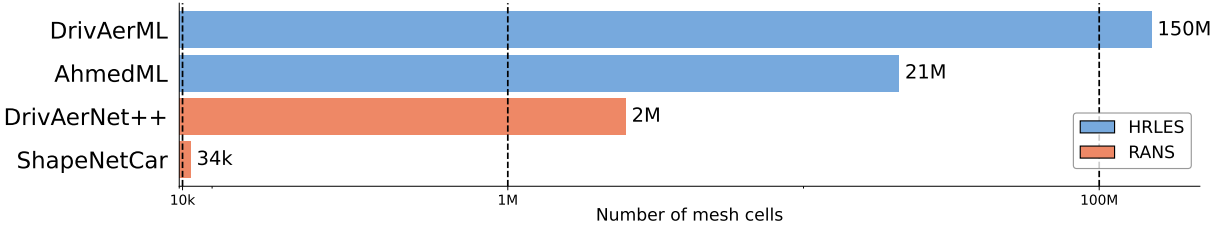


Figure 1: AB-UPT is a neural surrogate model trained to jointly model surface and volume variables of automotive CFD simulations with $> 100M$ simulation mesh cells. It obtains state-of-the-art surface and volume predictions (left), accurately models drag and lift coefficients (center) all on a single GPU (right).



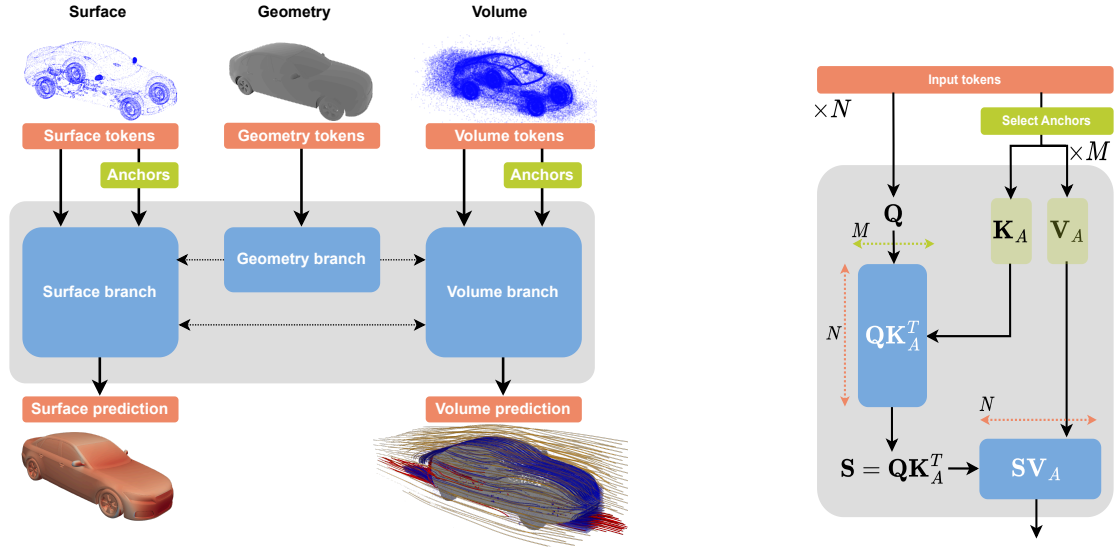
(a) **Triad of scales:** illustration of key scales in CFD surrogate modeling, placing special emphasis on the problem scale.

(b) **Problem scale** entails the fidelity of the numerical simulation and the complexity of the physics phenomena. Industry-standard simulations often use hundreds of millions of mesh cells to capture complex physics.



(c) The scale of CFD datasets in automotive aerodynamics, by the number of mesh cells.

Figure 2: We introduce *problem scale* in the context of computational fluid dynamics (CFD) simulations and develop a neural surrogate architecture that can handle data from publicly available CFD datasets that uses a high-fidelity CFD approach (HRLES) routinely employed in industry-standard automotive simulations.



(a) **Multi-branch architecture:** AB-UPT encodes geometries into a reduced set of latent geometry tokens that are integrated into predictions via cross-attention. Interactions between surface and volume fields are modeled via cross-attention.

(b) **Anchor attention:** Physics is approximated using latent anchor tokens that share context via self-attention. Predictions at additional query points cross-attend to anchor tokens.

Figure 3: Overview Anchored-Branched Universal Physics Transformers (AB-UPT).

In recent years, deep neural network-based surrogates have emerged as a computationally efficient alternative in science and engineering (Thuerey et al., 2021; Zhang et al., 2023; Brunton et al., 2020), impacting, e.g., weather forecasting (Pathak et al., 2022; Bi et al., 2023; Lam et al., 2023; Nguyen et al., 2023; Bodnar et al., 2025), protein folding (Jumper et al., 2021; Abramson et al., 2024), or material design (Merchant et al., 2023; Zeni et al., 2025; Yang et al., 2024). In many of these scientific disciplines, the Transformer architecture (Vaswani et al., 2017) has become a central backbone of the recent breakthroughs. Inherently linked to Transformers is the notion of *scale*, both in terms of trainable parameters of the model and the amount of data needed to train those scaled models. However, the notion of scale is ill-defined in the field of neural surrogate modeling for science and engineering, mainly due to the lack of availability of high-volume training data. Hence, we start this work by posing the following question:

How to define and harness *scale* in the context of (automotive) neural surrogates for CFD simulations?

Scaling large machine learning models is usually framed in terms of the number of trainable parameters and the overall dataset size. Particular to the CFD field, however, is the fact that industry-standard volumetric meshes often exceed more than 100 million cells (i.e., high-dimensional data), while at the same time the amount of simulation samples is low (i.e., low number of independent training samples). Moreover, intricate geometry-dependent interactions between the surface and volumetric fields govern the underlying physics. Further complexity arises from field quantities such as vorticity, which are highly nonlinear yet inherently divergence-free. The combination of high-dimensional non-linear physics phenomena and the low number of industry-standard training samples makes scaling neural surrogate models for CFD particularly hard. Thus, our definition of scale also encompasses *problem scale*, i.e. the fidelity of the simulation (visually represented in Figure 2). To harness problem scale, we propose Anchored-Branched Universal Physics Transformers (AB-UPT) (see Figure 3, a novel modeling scheme, build on the Universal Physics Transformer (UPT) framework, for building neural surrogates for automotive CFD simulations. The modeling is organized into three branches (geometry-encoding, surface-prediction, volume-prediction), with

Model	Computation unit	Paradigm	Accuracy	Context tokens	Speed (train)	Speed (test)	Simulation from CAD mesh	Neural field decoder
HRLES	Equations	Numeric	✓✓✓	-	-	✗✗	✗	-
RANS	Equations	Numeric	✓✓*	-	-	✗	✗	-
PointNet	MLPs	Point-based	✗✗	✗	✗	✓	✗	✗
GINO	GNO/FNO	Grid interpol.	✗	✗	✗	✓	✓	✓
OFormer	Lin. transformer	Point-based	✓	✗	✗	✓	✓	✓
Transolver	Lin. transformer	Point-based	✓	✗	✗	✓	✗	✗
AB-UPT	Transformer	Latent space	✓✓	✓	✓	✓	✓	✓

Table 1: Conceptual overview of different CFD solvers. Numeric integration schemes, while accurate, are slow and require specialized meshes to converge, with several orders of magnitude variations in fidelity and runtime. Neural surrogates struggle to be trained on the full-resolution mesh, which makes them slow to train or requires multi-GPU setups for million-scale meshes. Next to that, those methods require computation units that favor speed over accuracy. We introduce AB-UPT, a new method incorporating *anchor tokens*. AB-UPT unlocks linear problem scaling, which enables training of neural surrogates on a single GPU in less than a day, even on million-scale meshes. This efficiency also allows us to leverage expressive neural computation units such as the Transformer. Furthermore, our multi-branch design enables simulation with any input mesh, uses reduced latent modeling of physical dynamics. Finally, *anchor attention* acts as a neural field, enabling an efficient divergence-free vorticity field formulation. *We hypothesize that neural surrogates can produce results with an accuracy similar to RANS when trained on data from HRLES. However, such comparisons are difficult to make as there are no public datasets available which have paired RANS/HRLES results for the same large-scale geometries.

cross-attention between and self-attention within branches, decoupling feature extraction from field prediction. Within each branch, the encoded simulation points are partitioned into two sets: a small set of selected *anchor* tokens share information among each other via self-attention and together provide context (e.g., about the physical dynamics); the remaining *query* tokens only receive information from the anchor tokens via cross-attention, leading to independent query predictions. This anchor-based design has three critical advantages, resulting in strong generalization performance, inference efficiency, and physics consistency: (i) selecting subsets of points massively increases the amount of effective training instances, and the number of anchor tokens governs the model’s computational capacity; (ii) computational cost scales quadratically only with the small number of anchor tokens, while predictions on all other points have linear computational complexity; (iii) interpreting the anchor mechanism as a conditional-field model enables the application of differential operators, and we leverage this capability to derive a divergence-free vorticity-field formulation.

We demonstrate the effectiveness of AB-UPT by comparing its predictive performance against strong surrogate baselines on automotive CFD simulation tasks, including industrial-scale datasets. Key highlights include:

- (I) Training models in less than a day, predicting surface and volume fields in seconds on a single GPU.
- (II) State-of-the-art predictive accuracy on automotive CFD simulations with up to 140 million mesh cells.
- (III) Near-perfect accuracy in drag and lift coefficients computed from pressure predictions.
- (IV) Enabling continuous field predictions from CAD geometries, eliminating costly mesh creation.
- (V) Accurate and physically consistent vorticity predictions via divergence-free formulation.

2 Preliminaries and related work

We outline a conceptual overview and high-level description of our architecture AB-UPT in Table 1. This section provides background information for numerical solvers in Section 2.1 as well as for related work in neural surrogate modeling in Section 2.2. A detailed description of our method follows in Section 3.

2.1 CFD for automotive aerodynamics

Computational fluid dynamics. Automotive aerodynamics is centered around computational fluid dynamics (CFD) (Versteeg & Malalasekera, 2007; Hirsch, 2007; Pletcher et al., 2012), which is deeply connected to solving the Navier-Stokes (NS) equations. For automotive aerodynamics simulations, the assumptions of incompressible fluids due to low local Mach numbers, i.e., low ratio of flow velocity to the speed of sound, are justified (Ashton et al., 2024b). Thus, the simplified incompressible form of the NS equations (Temam, 2001) is applicable, which conserves momentum and mass of the flow field $\mathbf{u}(t, x, y, z) : [0, T] \times \mathbb{R}^3 \rightarrow \mathbb{R}^3$ via:

$$\frac{\partial \mathbf{u}}{\partial t} = -\mathbf{u} \cdot \nabla \mathbf{u} + \mu \nabla^2 \mathbf{u} - \nabla p + \mathbf{f}, \quad \nabla \cdot \mathbf{u} = 0. \quad (1)$$

To compute a numerical solution, it is essential to discretize the computational domain. In CFD, the finite volume method (FVM) is one of the most widely used discretization techniques. FVM partitions the computational domain into discrete control volumes using a structured or unstructured mesh. The initial geometric representation, typically provided as a computer-aided design (CAD) model in formats such as STL, must be transformed into a volumetric simulation mesh. This meshing process precisely defines the simulation domain, allowing the representation of complex flow conditions, such as those in wind tunnel configurations or open-street environments.¹ Note that meshing highly depends on the turbulence modeling and the flow conditions (Versteeg & Malalasekera, 2007).

Turbulence modeling in CFD. Turbulence arises when the convective forces $\mathbf{u} \cdot \nabla \mathbf{u}$ dominate over viscous forces $\mu \nabla^2 \mathbf{u}$, typically quantified by the Reynolds number. Turbulent flows are characterized by a wide range of vortices across scales, with energy cascading from larger structures to smaller ones until viscous dissipation converts it into thermal energy at the Kolmogorov length scale. Although direct numeric simulation (DNS) can theoretically resolve the turbulent flow field by directly solving the NS equations, it requires capturing all scales of motion down to the Kolmogorov scale. This implies extremely high requirements on the discretization mesh, which results in infeasible computational costs for full industrial cases (Versteeg & Malalasekera, 2007).

Therefore, engineering applications rely on turbulence modeling approaches that balance accuracy and computational efficiency. Reynolds-Averaged Navier-Stokes (RANS) (Reynolds, 1895; Alfonsi, 2009) and Large-Eddy Simulations (LES) (Lesieur et al., 2005) are two methods for modeling turbulent flows, each with distinct characteristics. RANS decomposes flow variables into mean and fluctuating components and solves the time-averaged equations, using turbulence models like k- ϵ (Lauder & Spalding, 1974) to account for unresolved fluctuations. While computationally efficient, RANS may lack accuracy in capturing complex or unsteady flows, particularly in cases involving flow separation, where turbulence models are often less effective. In contrast, LES resolves eddies down to a cut-off length and models sub-grid scale effects and their impact on the larger scales. LES offers higher accuracy in capturing unsteady behavior and separation phenomena at the cost of more compute. In cases where LES is too costly, hybrid models like, Hybrid RANS-LES (HRLES) models (Spalart et al., 2006; Chaouat, 2017; Heinz, 2020; Ashton et al., 2022) are an alternative. These models reduce computational demand by using LES away from boundary layers, and RANS near surfaces, where sufficiently resolving the flow in LES would require very high resolution. The DrivAerML (Ashton et al., 2024b) is currently the dataset with the highest fidelity that is publicly available. The dataset utilizes a HRLES turbulence model and runs CFD simulations on 140 million volumetric cells.

Quantities of interest. Interesting quantities for automotive aerodynamics comprise quantities on the surface of the car, in the volume around the car, as well as integral quantities such as drag and lift coefficients. The force acting on an object in an airflow is given by

$$\mathbf{F} = \oint_S -(p - p_\infty) \mathbf{n} + \boldsymbol{\tau}_w dS, \quad (2)$$

with the aerodynamic contribution, consisting of surface pressure p and pressure far away from the surface p_∞ times surface normals \mathbf{n} , and the surface friction contribution $\boldsymbol{\tau}_w$. For comparability between designs,

¹We emphasize the differentiation between raw *geometry mesh* and the re-meshed *simulation mesh* for CFD modeling.

dimensionless numbers as drag and lift coefficients

$$C_d = \frac{2 \mathbf{F} \cdot \mathbf{e}_{\text{flow}}}{\rho v^2 A_{\text{ref}}}, \quad C_l = \frac{2 \mathbf{F} \cdot \mathbf{e}_{\text{lift}}}{\rho v^2 A_{\text{ref}}} \quad (3)$$

are used (Ashton et al., 2024b), where \mathbf{e}_{flow} is a unit vector into the free stream direction, \mathbf{e}_{lift} a unit vector into the lift direction perpendicular to the free stream direction, ρ the density, v the free stream velocity, and A_{ref} a characteristic reference area. Predicting these surface integrals allows for an efficient estimation when using deep learning surrogates, since these surrogates can directly predict the surface values without the need to model the full 3D volume field, as required by numerical CFD simulations.

Conserved quantities. The vorticity field, defined as the curl of the velocity field, i.e., $\boldsymbol{\omega} = \nabla \times \mathbf{u}$, is inherently divergence-free due to the mathematical identity that the divergence of a curl is always zero, i.e., $\nabla \cdot \boldsymbol{\omega} = \nabla \cdot \nabla \times \mathbf{u} = 0$. However, it is crucial to distinguish the divergence-free property of the vorticity field from the incompressible formulation of the Navier–Stokes equations, where the divergence-free condition applies directly to the velocity field as a consequence of mass conservation in an incompressible (constant-density) fluid, i.e., $\nabla \cdot \mathbf{u} = 0$. In the context of the vorticity formulation, the divergence-free condition arises from the definition of vorticity and does not imply or enforce incompressibility of the underlying velocity field.

2.2 Transformer blocks for building neural surrogates

Neural surrogates. Many neural surrogate models are formulated in the neural operator learning paradigm (Lu et al., 2021a; Li et al., 2020; 2021; Seidman et al., 2022; Alkin et al., 2024a;b). In this framework, neural networks represent operators that map between Banach spaces \mathcal{I} and \mathcal{O} of functions defined on compact domains \mathcal{X} and \mathcal{Y} , i.e., $\mathcal{G} : \mathcal{I} \rightarrow \mathcal{O}$. Neural operators provide continuous outputs that remain consistent across varying input sampling resolutions and patterns. Training a neural operator involves constructing a dataset of input-output function pairs evaluated at discrete spatial locations.

AB-UPt is a neural operator that can encode different input representations (e.g., simulation surface mesh, geometry mesh) via the flexible multi-branch architecture and produce outputs of arbitrary resolution via *anchor attention*.

Self-attention and cross-attention. Scaled dot-product attention (Vaswani et al., 2017) is defined upon query $\mathbf{Q}(\mathbf{Z}) \in \mathbb{R}^{N \times d}$, key $\mathbf{K}(\mathbf{Z}) \in \mathbb{R}^{N \times d}$ and value $\mathbf{V}(\mathbf{Z}) \in \mathbb{R}^{N \times d}$ matrices which are linear projections from a latent representation $\mathbf{Z} \in \mathbb{R}^{N \times d}$, written in matrix representation as $\text{Attention}(\mathbf{Q}, \mathbf{K}, \mathbf{V}, \mathbf{Z}) = \text{softmax}(\mathbf{Q}(\mathbf{Z})\mathbf{K}(\mathbf{Z})^T / \sqrt{d})\mathbf{V}(\mathbf{Z})$, where N is the number of tokens and d is the hidden dimension.

Cross-attention is a variant of scaled dot-product attention where a second latent representation $\mathbf{Z}_{KV} \in \mathbb{R}^{M \times d}$ is used as input to $\mathbf{K}(\cdot)$ and $\mathbf{V}(\cdot)$. Intuitively, this formulation incorporates information from \mathbf{Z}_{KV} into \mathbf{Z} . It is commonly used to enable interactions between different modeling components (e.g., Vaswani et al. (2017)), data types (e.g., Alayrac et al. (2022)), or to compress/expand representations (e.g., Jaegle et al. (2021)). Roughly speaking, the first two use-cases use $N \approx M$ whereas the third use-case uses $N \ll M$ (compression) or $M \ll N$ (expansion).

AB-UPt uses self-attention throughout the whole model to exchange global information between tokens, cross-attention with geometry tokens as keys/values to incorporate geometry information into the surface/volume branches, and cross-attention between branches to enable surface-volume interactions.

Neural field output decoding via cross-attention. Neural fields (Mildenhall et al., 2020) are neural networks that take continuous coordinates as inputs and produce a prediction for this exact coordinate. The continuous nature of the input coordinates enables evaluating this function at arbitrary positions, making it a field. By using embedded coordinates as \mathbf{Z} and a latent representation of, e.g., the simulation state as \mathbf{Z}_{KV} , cross-attention acts as a conditional neural field (Wang et al., 2024b) as each query vector retrieves information from the latent representation to produce a prediction for a given query coordinate. It is worth noting that the neural field decoding via cross-attention operates on a point-wise basis, and hence, is independent of the number of query points.

Neural field decoding approaches have been commonly utilized in the context of neural surrogates (Li et al., 2023a; Alkin et al., 2024a; Wang et al., 2024b) to produce high-resolution outputs from a latent representation.

AB-UPT also utilizes a neural field decoder via cross-attention. Contrary to previous methods, our decoder can use a more expressive context as expressive self-attention is employed between anchor tokens, where all anchor tokens (including intermediate representations) serve as a condition for the neural field decoder.

2.3 Related work

In this section, we will discuss work related to neural surrogate modeling for aerodynamics.

Reduced latent space modeling. Training neural surrogates directly on a complete simulation mesh can be computationally expensive and, in some cases, even infeasible. To address this issue, compression of the input mesh into a reduced latent space can be employed. Next, a decoder (often functioning as a point-wise decoder) needs to be able to reconstruct the output mesh conditioned on the compressed latent representation and single query points. To satisfy this requirement, the decoder must function as a conditional neural field. Such approaches are introduced in AROMA (Serrano et al., 2024), CViT (Wang et al., 2024b), Knigge et al. (2024), GOAT Wen et al. (2025), LNO (Wang & Wang, 2024), and UPT (Alkin et al., 2024a). Moreover, UPT additionally introduces a patch-embedding analogue for compressing general geometries via supernode pooling.

Unreduced physics modeling. Methods like Reg-DGCNN (Wang et al., 2019; Elrefaie et al., 2024a;b), Graph-UNet Gao & Ji (2019), PointNet (Qi et al., 2017a), and transformer models with linear complexity, such as FactFormer (Li et al., 2024), GNOT (Hao et al., 2023), ONO (Xiao et al., 2023), OFormer (Li et al., 2023a) or Transolver (Wu et al., 2024) have constant compute complexity w.r.t. the number of input points. This allows such models to process the unreduced simulation mesh at high computation costs, as shown in Transolver++ (Luo et al., 2025), which demonstrates processing meshes with 2.5 million cells via sequence parallelism on four GPUs. Although technically feasible, such approaches also become infeasible at larger scales. For example, linearly extrapolating the reported GPU requirements of Transolver++ would necessitate roughly 256 GPUs to process a simulation mesh with 140 million cells. In contrast, AB-UPT can process simulations of 140 million cells on a single GPU.

Decoupling of encoder and decoder. Decoupling encoding and decoder components is often beneficial for tasks like predicting 3D flow fields directly from geometric inputs (see e.g., GINO (Li et al., 2023b), GOAT Wen et al. (2025), LNO Wang et al. (2024a), OFormer (Li et al., 2023a), and UPT). Additionally, a decoupled latent space representation allows for scalable decoding to a large number of output mesh cells since such models can cache encoded latent states and decode output queries in parallel. Moreover, decoupling the encoder and decoder also allows for independent input and output meshes. This means the model does not require the same simulation mesh used for ground truth output as its encoder input during training (i.e., the encoder can be simulation mesh independent), providing greater flexibility in data handling.

Hard physical constraints in neural networks. Physics-Informed Neural Networks (PINN) (Raissi et al., 2019) are a popular approach for learning neural networks that enforce the governing equations by adding the residuals of the partial differential equation (PDE) and boundary conditions as *soft* penalty terms in the loss function. It has been shown that these methods require second-order optimization methods to learn from the otherwise conflicting signal in the data and the soft constraints Wang et al. (2025). In this work, we instead use the conditional field property of our model to directly incorporate physical properties into the architecture itself as a *hard* constraint. Related approaches (i.e., (Lu et al., 2021b; Richter-Powell et al., 2022)) are much less common and have so far not been scaled to the massive model, data, and problem scales considered in this work.

3 Anchored-Branched Universal Physics Transformers

We introduce Anchored-Branched Universal Physics Transformers (AB-UPT), which leverages two key modeling components: (i) the *multi-branch* architecture outlined in Section 3.1 separates geometry encoding, surface-level simulation, and volume-level simulation into distinct branches that interact with each other; (ii) *anchor attention* described in Section 3.2 enables modeling of complex physical dynamics by leveraging expressive dot-product attention (Vaswani et al., 2017) within a heavily reduced set of *anchor tokens*. To generate predictions for the full simulation mesh during inference, *anchor attention* employs cross-attention

between (millions) of *query tokens* and the small amount of *anchor tokens*, which has linear inference complexity. Additionally, *anchor attention* can be seen as a conditional neural field, which allows creating arbitrary output resolutions, and enables the application of differential operators to enforce hard physical constraints such as divergence-free vorticity-field predictions (see Section 3.3).

3.1 Multi-branch architecture

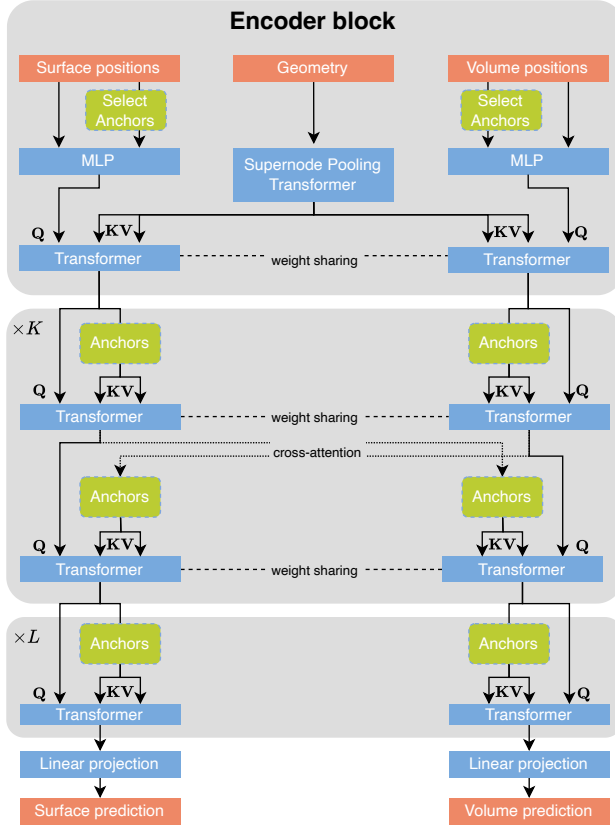


Figure 4: The Anchored-Branched Universal Physics Transformers model is a multi-branch Transformer neural operator using three distinct branches: a surface, geometry, and volume branch. The physics blocks within each branch share parameters and interact through cross-attention. To handle problems at industry-scale, we select a subset of M points from the input point cloud. We call these points *anchor tokens*, and they serve as the keys and values for attention computation. This approach significantly reduces the complexity of attention, making it possible to scale our model to industry-standard simulation meshes.

Our model builds on the Universal Physics Transformer (UPT) (Alkin et al., 2024a) and multi-branch Transformers for neural operators (Alkin et al., 2024b; Esser et al., 2024). Multi-branch Transformers consist of multiple branches (which can share parameters) that each handle different data streams or modalities. We define a geometry branch, a surface branch, and a volume branch (see Figures 3 and 4 for an overview). Those branches interact differently in respective encoding, physics, and decoding blocks, and allow us to enable scalability to high-resolution outputs via the new *anchor attention*. We distinguish the geometry, surface, and volume branches by the superscripts g , s , and v , respectively.

Multi-branch encoder block. The geometry branch encodes an arbitrary input geometry \mathcal{M} (which can be different than the simulation mesh), from a simulation sample, which is represented as a finite discretized

point cloud, consisting of N^g points in a 3D space, i.e., $\mathbf{X}^g \in \mathbb{R}^{N^g \times 3}$. The 3D coordinates are embedded using the Transformer positional encoding (Vaswani et al., 2017). We found that no additional input features are required for any of the branches. However, we note that it is possible to add additional inputs such as surface normals, signed distance function (SDF) features, or simulation design parameters. Following the approach of Alkin et al. (2024a), a supernode pooling block \mathcal{S} maps the input geometry \mathcal{M} into a reduced set of supernode representations \mathbf{S} , which capture local geometry information within some radius r of the supernode:

$$\mathcal{S} : \mathbf{X}^g \in \mathcal{M} \xrightarrow{\text{Embed}} \mathbf{H}^g \in \mathbb{R}^{N^g \times d} \xrightarrow{\text{Supernode pooling}} \mathbf{S} \in \mathbb{R}^{S \times d}, \quad (4)$$

where d is the dimensionality of the model's latent representations. Distances in the supernode pooling are computed only based on the input coordinates: first, we sample a subset of S supernodes, where typically $S \ll N^g$, from the coordinates \mathbf{X}^g . Through a Graph Neural Operator (GNO) layer (Li et al., 2020), we aggregate information from neighboring coordinates within a radius r . The resulting supernode representations \mathbf{S} are passed through a self-attention block, allowing the supernodes to aggregate global information from the other supernodes, resulting in the output of the geometry branch

$$\mathcal{G} : \mathbf{S} \xrightarrow{\text{Attention}} \mathbf{Z}^g \in \mathbb{R}^{S \times d}. \quad (5)$$

We discretize the input of the surface and volume branches by turning the simulation mesh into sets of 3D point clouds. Specifically, we select N^s points from the surface and N^v points in the 3D volume, i.e., $\mathbf{X}^s \in \mathbb{R}^{N^s \times 3}$ and $\mathbf{X}^v \in \mathbb{R}^{N^v \times 3}$. To embed the 3D coordinates, we use the Transformer positional encoding as in the geometry branch. Then, we encode these embedded points by using two multi-layer perceptron (MLP) encoders, \mathcal{E}^s and \mathcal{E}^v . We employ separate MLP encoders for surface coordinates (\mathcal{E}^s) compared to volume coordinates (\mathcal{E}^v) to provide explicit contextual information, designating which points reside on the surface and within the volume. To summarize, the surface and volume encoder are defined as follows:

$$\mathcal{E}^s : \mathbf{X}^s \xrightarrow{\text{Embed}} \mathbf{H}^s \xrightarrow{\text{MLP}} \mathbf{Z}^s \in \mathbb{R}^{N^s \times d}, \quad (6a)$$

$$\mathcal{E}^v : \mathbf{X}^v \xrightarrow{\text{Embed}} \mathbf{H}^v \xrightarrow{\text{MLP}} \mathbf{Z}^v \in \mathbb{R}^{N^v \times d}. \quad (6b)$$

Multi-branch physics blocks and decoder. To bridge the geometry and the surface/volume branch, we use a cross-attention block, \mathcal{P}^s and \mathcal{P}^v , which shares parameters among the surface and volume branches.

$$\mathcal{P}^s : (\mathbf{Q}(\mathbf{Z}^s), \mathbf{K}(\mathbf{Z}^g), \mathbf{V}(\mathbf{Z}^g)) \xrightarrow{\text{Attention}} \mathbf{Z}_0^s, \quad (7a)$$

$$\mathcal{P}^v : (\mathbf{Q}(\mathbf{Z}^v), \mathbf{K}(\mathbf{Z}^g), \mathbf{V}(\mathbf{Z}^g)) \xrightarrow{\text{Attention}} \mathbf{Z}_0^v, \quad (7b)$$

where we write $\mathbf{Q}(\mathbf{Z})$, $\mathbf{K}(\mathbf{Z})$ and $\mathbf{V}(\mathbf{Z})$ to denote the linear transformation from representation \mathbf{Z} to its corresponding query, key and value matrix. The queries are the encoded surface and volume points, and the output of the geometry branch serves as keys and values. This setup enables the surface and volume points to effectively incorporate information from the geometry encoder, providing global information about the input geometry.

The surface and volume branch consists of K physics blocks. Each physics block k , where $k \in \{1, \dots, K\}$, consists of a self-attention and cross-attention block, which share parameters between the surface and volume branches. Each physics block starts with a self-attention block, where the queries, keys, and values are all derived from the output \mathbf{Z}_{k-1} of the preceding physics block $k-1$, where \mathbf{Z}_0 from Equation (7) is the input to the first block. Next is a cross-attention block, enabling surface-volume interaction. For the surface branch, the queries originate from the previous block within the surface branch. However, the keys and values come from the volume branch k . For the volume branch, however, it is reversed: the queries come from the volume branch, and the keys and values from the surface branch. These cross-attention layers allow for intricate interactions between the surface and volumetric fields. Formally, physics block k for the surface and volume branch, \mathcal{B}_k^s and \mathcal{B}_k^v , are defined by:

$$\mathcal{B}_k^s : \{\mathbf{Q}(\mathbf{Z}_{k-1}^s), \mathbf{K}(\mathbf{Z}_{k-1}^s), \mathbf{V}(\mathbf{Z}_{k-1}^s)\} \xrightarrow{\text{Attention}} \mathbf{Z}_k'^s \rightarrow \{\mathbf{Q}(\mathbf{Z}_k'^s), \mathbf{K}(\mathbf{Z}_k^v), \mathbf{V}(\mathbf{Z}_k^v)\} \xrightarrow{\text{Attention}} \mathbf{Z}_{k+1}^s, \quad (8a)$$

$$\mathcal{B}_k^v : \{\mathbf{Q}(\mathbf{Z}_{k-1}^v), \mathbf{K}(\mathbf{Z}_{k-1}^v), \mathbf{V}(\mathbf{Z}_{k-1}^v)\} \xrightarrow{\text{Attention}} \mathbf{Z}_k'^v \rightarrow \{\mathbf{Q}(\mathbf{Z}_k'^v), \mathbf{K}(\mathbf{Z}_k^s), \mathbf{V}(\mathbf{Z}_k^s)\} \xrightarrow{\text{Attention}} \mathbf{Z}_{k+1}^v. \quad (8b)$$

The final decoder block consist of L self-attention blocks that do not share parameters and hence operate independently. The query, key, and value representations all originate from the previous layer, and, therefore, there is no interaction anymore between the two branches. This design allows for branch-specific modeling, meaning each branch can refine the output predictions independently, without interaction with the other branches. Finally, a single linear projection is applied as a decoder to generate the final output predictions for each branch.

We use a standard pre-norm transformer architecture akin to Vision Transformers (Dosovitskiy et al., 2021) where each attention block is followed by an MLP block (which we omit above for notational simplicity). Additionally, we employ Rotary Position Embeddings (RoPE) (Su et al., 2024) in all attention blocks.

3.2 Anchor attention

High-fidelity numerical simulations in industry often rely on extremely fine mesh discretizations, sometimes comprising hundreds of millions of cells (Ashton et al., 2024b). In practice, representing such large point clouds (meshes) as inputs to surrogate models becomes computationally challenging. In particular, Transformer models (Vaswani et al., 2017)—the workhorse of many modern deep learning architectures—capture dependencies among all N input tokens via self-attention:

$$\text{Attention}(\mathbf{Q}(\mathbf{Z}), \mathbf{K}(\mathbf{Z}), \mathbf{V}(\mathbf{Z})) = \text{softmax} \left(\frac{\mathbf{Q}(\mathbf{Z})\mathbf{K}(\mathbf{Z})^\top}{\sqrt{d}} \right) \mathbf{V}(\mathbf{Z}) .$$

Because forming the full $\mathbf{Q}(\mathbf{Z})\mathbf{K}(\mathbf{Z})^\top$ matrix takes $\mathcal{O}(N^2)$ time and memory, this operation becomes infeasible when N is on the order of hundreds of millions.

To mitigate this problem, we introduce the concept of *anchor attention*, which splits the discretized input mesh (i.e., the point cloud) into two parts: (i) a small subset \mathbf{A} of M *anchor tokens* is uniformly sampled from the N input tokens and used to derive the key matrix $\mathbf{K}(\mathbf{A})$ and value matrix $\mathbf{V}(\mathbf{A})$ for the attention mechanism; (ii) the query matrix $\mathbf{Q}(\mathbf{Z})$, which is derived from *all* N input tokens, then cross-attend to the anchor key and value matrices. Intuitively, this formulation splits the N input tokens into M *anchor tokens* (used as queries, keys and values in the attention) and $N - M$ *query tokens* (used only as queries in the attention). It is equivalent to self-attention within the M *anchor tokens* and cross-attention between $N - M$ *query tokens* and the M *anchor tokens*. Formally, anchor attention is defined as follows:

$$\begin{aligned} \mathcal{I}_A &\sim \text{UniformSample}(\{1, 2, \dots, N\}, M) & M \ll N, \\ \mathbf{A} &= \mathbf{Z}[\mathcal{I}_A] & \in \mathbb{R}^{M \times d}, \\ \text{AnchorAttention}(\mathbf{Q}(\mathbf{Z}), \mathbf{K}(\mathbf{A}), \mathbf{V}(\mathbf{A})) &= \text{softmax} \left(\frac{\mathbf{Q}(\mathbf{Z})\mathbf{K}(\mathbf{A})^\top}{\sqrt{d}} \right) \mathbf{V}(\mathbf{A}) & \in \mathbb{R}^{N \times d}, \end{aligned} \quad (9)$$

where \mathcal{I}_A is sampled once for every sample in a forward pass.

This design allows us to *focus on problem scale* (c. f. Figure 2): by choosing the number of anchor tokens M , we directly control the model’s computational capacity, while enabling pointwise predictions at arbitrary points in the continuous output domain. These anchor tokens span both the surface and volume mesh, and their selection is crucial for capturing problem-specific structure. Increasing M enhances contextual information available at each query location without changing the amount of model parameters, thereby improving performance up to a saturation point (see Figure 5).

Importantly, the $N - M$ query tokens only need to compute attention with a much smaller set of M key-value pairs (derived from the anchor tokens) compared to full self-attention, which computes all N^2 pairs. Anchor attention therefore *reduces the computational complexity* of the attention layers from $\mathcal{O}(N^2)$ to $\mathcal{O}(M^2 + (N - M)M) = \mathcal{O}(MN)$, where M^2 is the self-attention between the M anchor tokens and $(N - M)M$ is the cross-attention from $N - M$ query tokens to M anchor tokens. This is crucial because surrogate models often need to be evaluated at a large number of input points (e.g., to obtain accurate drag/lift coefficient predictions as shown in Figure 1). Additionally, since there are no interactions between

query tokens, arbitrary many query tokens can be used per forward pass. Therefore, query tokens can be processed in chunks, enabling constant memory consumption by using a constant amount of queries. When processing all N input tokens at once (*end-to-end inference*), memory complexity of anchor attention is $\mathcal{O}(N)$ (we use an efficient attention implementation (Dao et al., 2022)). However, as N can be $> 100M$, it would still run into out-of-memory errors on a single GPU. By chunking the $N - M$ query tokens into chunks of size C , memory complexity reduces to $\mathcal{O}(M + C)$, i.e., constant memory consumption. We refer to this methodology as *chunked inference* (c.f. inference memory in Figure 1). Moreover, in chunked inference, the key-value pairs of anchor tokens can be cached when calculating them in the first chunked forward pass to omit recalculating them for subsequent chunks (anchor tokens remain constant for all chunks). However, as $M \ll N$, this is often negligible.

Finally, by treating the anchors as conditioning set for the queries, anchor attention turns the architecture into a *conditional field model*: the field values at any query location are predicted from the query location itself and the context provided by the anchors, but independently from any other query location. This has two important benefits. First, this enables creating predictions at arbitrary query positions, which allows AB-UPT to predict at arbitrary resolution. Many simulation insights can be obtained from much lower resolutions than necessary for numeric simulation (e.g., drag/lift coefficients in Figure 6). Second, it allows us to impose physics-based constraints directly into the model predictions, such as a divergence-free condition for vorticity (see Section 3.3).

3.3 Enforcing physics consistency

Anchored neural field enables derivative operators. As discussed in Section 2.1, physical fields are often intrinsically governed by local differential operators, enforcing constraints that reflect fundamental conservation laws. However, imposing differential-operator constraints on neural networks requires a field-based formulation, allowing *pointwise* derivative computation. Conventional Transformer architectures cannot be directly viewed as continuous fields because they map input sets to output sets. By contrast, as described in Section 3.2, our anchored neural field architecture treats the network as a conditional field, using anchor tokens’ key/value vectors as the context to produce pointwise predictions at arbitrary query positions. This approach enables the application of local differential operators. To demonstrate and leverage the potential of the anchored-field formulation, we model the vorticity as an intrinsically divergence-free field, constructed from the local rotation of the velocity (like the real physical field), thus ensuring physical consistency.

Divergence-free vorticity field. Let $\mathbf{u} : \mathbb{R}^3 \rightarrow \mathbb{R}^3$ be the velocity field and denote its value at any point $\mathbf{x} = (x_1, x_2, x_3)$ by $\mathbf{u}(\mathbf{x})$. The local rotation of the velocity field is characterized by the *vorticity*, which is defined as the curl of the velocity:

$$\boldsymbol{\omega}(\mathbf{x}) = \nabla \times \mathbf{u}(\mathbf{x}) = \begin{pmatrix} \frac{\partial u_3}{\partial x_2} - \frac{\partial u_2}{\partial x_3} \\ \frac{\partial u_1}{\partial x_3} - \frac{\partial u_3}{\partial x_1} \\ \frac{\partial u_2}{\partial x_1} - \frac{\partial u_1}{\partial x_2} \end{pmatrix}. \quad (10)$$

A well-known mathematical property of the vorticity (and more generally the curl of a field) is that its divergence vanishes, i.e., $\nabla \cdot (\nabla \times \mathbf{u}) = 0$. Intuitively, this means that vorticity has no monopole-like sources or sinks: vortex lines can only form closed loops or extend to infinity, never beginning or ending at a point.

Models that directly predict the vorticity field $\hat{\boldsymbol{\omega}}(\mathbf{x})$ without further structure cannot guarantee $\nabla \cdot \hat{\boldsymbol{\omega}} = 0$, and thus lead to unphysical predictions that introduce spurious sources and sinks of vorticity. PINN typically address this by incorporating the residuals of the PDE and boundary conditions into the loss function as *soft constraints*. By contrast, we enforce the divergence-free condition as an architectural *hard constraint* by explicitly parameterizing the vorticity field as $\hat{\boldsymbol{\omega}}(\mathbf{x}) = \nabla \times \hat{\mathbf{u}}(\mathbf{x})$, where $\hat{\mathbf{u}}$ is the modeled velocity field. In other words, we define the vorticity as the curl of the modeled velocity field, which guarantees $\nabla \cdot \hat{\boldsymbol{\omega}} = 0$ by construction.

Finite-difference curl approximation. We found that computing the spatial derivatives in Equation (10) via PyTorch’s automatic differentiation is inefficient due to suboptimal support of vectorized cross-attention in

`torch.compile`. We therefore instead compute the spatial derivatives with a central-difference approximation,

$$\frac{\partial \hat{u}_i}{\partial x_j}(\mathbf{x}, \cdot) \approx \frac{\hat{u}_i(\mathbf{x} + \delta \mathbf{e}_j, \cdot) - \hat{u}_i(\mathbf{x} - \delta \mathbf{e}_j, \cdot)}{2\delta}, \quad (11)$$

where \hat{u}_i is the i -th (scalar) velocity output, \mathbf{e}_j is the unit vector in the x_j -direction, and δ is the step-size. Here, the dot in $\hat{\mathbf{u}}(\mathbf{x}, \cdot)$ indicates that the prediction also depends on additional inputs such as the anchor token’s key and value vectors, which we omit for notational simplicity. To approximate the partial derivatives w.r.t. each of the three spatial coordinates, we perform six additional forward passes, each applying an offset $+\delta \mathbf{e}_j$ and $-\delta \mathbf{e}_j$ to the input position.

Correcting for data normalization. In order to effectively train neural networks, input and target data is usually shifted and scaled into some appropriate range. Since the vorticity is defined through spatial derivatives of velocities w.r.t. the input coordinates in the raw *physics space*, the effect of scaling must be taken into account. This is because we compute the spatial derivatives of the neural network, i.e. in *network space*. Hence, when scaling the 3D input positions by a vector \mathbf{a} (from physics to network space) and the outputs by vector \mathbf{b} (from network to physics space), then the 3×3 network-space Jacobian matrix of partial derivatives must be multiplied by the outer-product matrix $\mathbf{b}\mathbf{a}^T$, resulting in the physics-space Jacobian.

4 Experiments

We begin our experiments by showing that neural surrogates do not need to process the full mesh to obtain accurate models (Section 4.2), which enables efficient training on large problem-scales. Using this insight, we design Anchored-Branched Universal Physics Transformers (AB-UPT) by adapting the UPT architecture (Alkin et al., 2024a) to handle complicated physical dynamics of CFD simulations with million-scale meshes (Section 4.3). To demonstrate the effectiveness of AB-UPT, we compare it against other neural surrogate models in Section 4.4. Finally, we demonstrate how AB-UPT can tackle practical use-cases such as calculating aerodynamic drag and lift coefficients (Section 4.5), simulating directly from a CAD geometry without the expensive creation of a simulation mesh (Section 4.6) as well as enforcing physical consistency via a divergence-free vorticity formulation (Section 4.7). Additional experiments are provided in Appendix A. The experimental setup for AB-UPT is outlined in Appendix B.3

4.1 Datasets

We consider three computational fluid dynamics datasets for automotive aerodynamics: ShapeNet-Car (Umetani & Bickel, 2018), AhmedML (Ashton et al., 2024a), and DrivAerML (Ashton et al., 2024b). Table 2 outlines properties of these datasets.

Table 2: Overview of considered datasets. Datasets vary in the number of surface/volume points (#Points) and their variables. High-quality datasets contain surface pressure \mathbf{p}_s and wallshearstress τ_w as well as volume pressure \mathbf{p}_v , velocity \mathbf{u} and vorticity ω . As CFD simulations are expensive to compute and store, these datasets do not contain many simulations, which also need to be split into train/validation/test splits.

Dataset	Surface			Volume				Properties		
	#Points	\mathbf{p}_s	τ_w	#Points	\mathbf{p}_v	\mathbf{u}	ω	#Simulations	Size	Cost ²
ShapeNetCar	4K	✓	✗	29K	✗	✓	✗	789/0/100	1 GB	<\$1K
AhmedML	1M	✓	✓	21M	✓	✓	✓	400/50/50	409 GB	\$200K
DrivAerML	9M	✓	✓	142M	✓	✓	✓	400/34/50	2677 GB	\$1M

4.2 Efficient training on million-scale CFD meshes

Numerical simulations require fine-grained meshes with sophisticated meshing algorithms to keep the numerical solver stable and obtain accurate results. Contrarily, neural surrogates, i.e., neural approximations of a

²Cost estimated with \$3 per Amazon EC2 `hpc6a.x48xlarge` node-hour which was used for both AhmedML and DrivAerML. This is the publicly visible on-demand hourly rate. Actual costs may vary based on instance provisioning model.

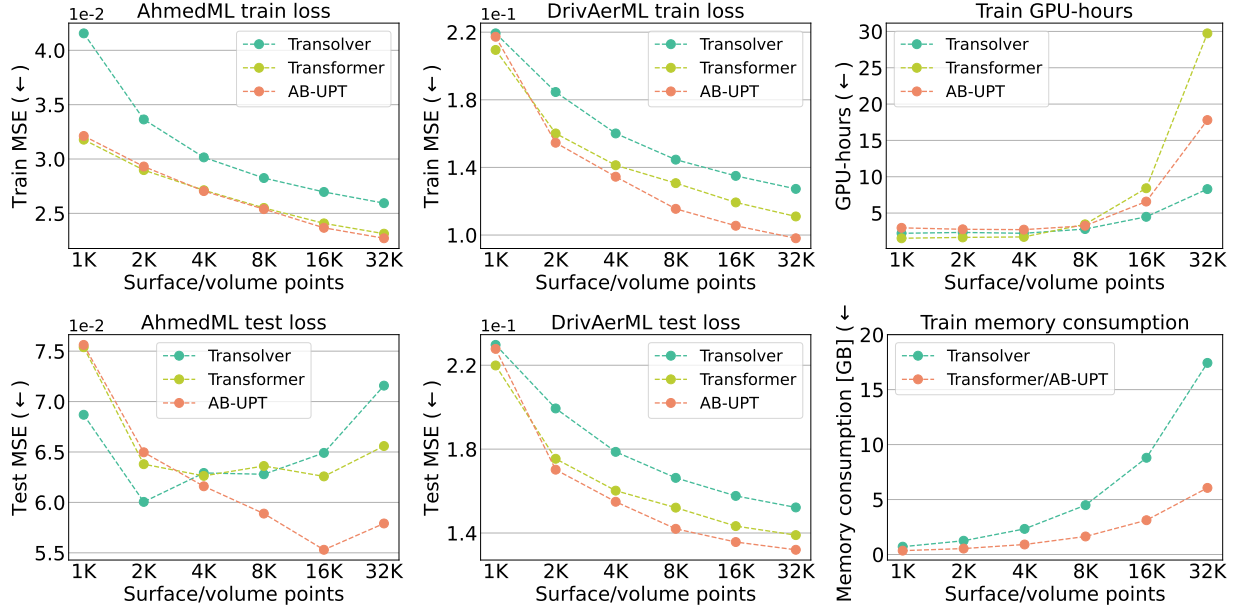


Figure 5: Train and test losses with varying number of training inputs. Contrary to numerical solvers, neural surrogates do not require million-scale meshes to train accurate models. Training on more points beyond a dataset-specific threshold results in overfitting and requires larger datasets (either in terms of data-scale, i.e., number of simulations or problem-scale, i.e., complexity of the problem) to benefit from the increased modeling capacity when using more points, which is costly. This can be observed in the first and second row where AhmedML and DrivAerML have the same data scale (400 train simulations) but AhmedML has smaller problem scale, resulting in overfitting. Note that increasing data- or model-scale is orthogonal to our work. Although runtime increases with a larger number of inputs, the amount of GPU-hours required is still low, and scaling to even larger problem-scales could be easily implemented via sequence parallelism (Liu et al., 2023), which allows scaling quadratic self-attention to millions of tokens.

numerical simulation, learn a conceptually different way of resolving the physical dynamics in a system. Consequently, we question the necessity of the fine-grained million-scale input mesh for a neural simulation by training neural surrogates with various input resolutions by randomly subsampling the CFD mesh. Figure 5 shows that the accuracy of a neural solver saturates at relatively coarse resolutions, where increasing resolution beyond a dataset-dependent threshold only increases computational costs without (test) accuracy gains. We use this insight to efficiently train neural surrogate models on meshes up to 140 million volume points by drastically reducing the input resolution and modeling physical dynamics in this reduced input space. This allows training models in less than a day on a single NVIDIA H100 GPU.

While such approaches have been explored in the past (Alkin et al., 2024a;b), many neural surrogate architectures focus on linear attention mechanisms (Li et al., 2023a; Wu et al., 2024) or computation parallelization (Luo et al., 2025) to be able to train with millions of inputs. However, such approaches would still be prohibitively expensive. For example, extrapolating the reported GPU requirements for training Transolver++ (Luo et al., 2025) to the 140 million inputs poings from DrivAerML (Ashton et al., 2024b) would necessitate roughly 256 GPUs.

We show in Figure 5 that it is feasible to train standard transformer self-attention to accurately predict simulation results on million-scale meshes by training on lower resolutions, outperforming linear attention architectures (such as Transolver). As self-attention requires quadratically more compute w. r. t. the number of inputs, computational demands increase. However, the number of GPU-hours required to train models is still low (models with 16 thousand surface/volume points train in less than 10 GPU-hours). Given even more complicated physical simulations, it would be no issue to scale our AB-UPT to more GPUs via sequence parallelism (Liu et al., 2023), which distributes tokens among multiple GPUs, to allow processing millions of

tokens despite the quadratic complexity of self-attention. Due to the low amount of GPU-hours required, even for physical dynamics that arise from meshes with over 100 million cells, there would be no issue with scaling our model to even more complicated problems. For reference, foundation models in domains such as computer vision (e.g., [Oquab et al. \(2023\)](#)) use 10 to 100 thousand GPU-hours, and compute requirements for language models can be millions of GPU-hours (e.g., [Dubey et al. \(2024\)](#)).

Note that random subsampling as we apply to create a low-resolution input mesh, is also a form of data augmentation where a network will never see the same constellation of inputs twice during training. As high-quality numerical CFD simulations are expensive to obtain (e.g., DrivAerML costs \$1M, see Table 2), datasets often have less than a thousand samples, where this form of regularization helps to prevent overfitting.

4.3 Model design

We design AB-UPT, a successor of UPT that preserves useful properties of UPT, such as using a neural field for decoding and being mesh independent (i.e., the input is decoupled from the output). We observe (in Table 3) that UPT is not able to model complicated dynamics such as the vorticity well, and gradually change the UPT architecture to employ techniques that allow efficient scaling to large problem sizes and obtain significantly higher accuracies than a vanilla UPT. We visualize design choices in Table 3 and motivate the design decisions below.

Table 3: Impact of design steps for transforming UPT into AB-UPT. Performance is measured as relative L2 error (in %) for surface pressure \mathbf{p}_s , volume velocity \mathbf{u} and volume vorticity ω . Train speed measures seconds per 100 update steps with batch size 1. Test speed measures seconds to create a prediction for the full simulation mesh. Speeds are measured on a NVIDIA H100 GPU. The study is conducted on AhmedML.

		L2 error (↓)			Neural field	Mesh independent	Train speed	Test speed
		\mathbf{p}_s	\mathbf{u}	ω				
baseline	UPT	4.51	3.26	51.06	✓	✓	7.0	0.2
macro design	+ large decoder	3.90	2.62	13.69	✓	✓	14.7	1.4
	+ decoder-only with self-attn	3.42	2.15	6.67	✗	✗	14.9	163
re-add properties	+ anchor attention	3.42	2.15	6.67	✓	✗	14.9	2.6
	+ decouple geometry encoding	3.20	2.01	6.47	✓	✓	16.1	2.5
micro design	+ split surface/volume branch	3.50	2.08	6.62	✓	✓	11.0	1.5
	+ cross-branch interactions	3.24	2.00	6.69	✓	✓	11.0	1.5
	+ branch-specific decoders	3.14	1.93	6.46	✓	✓	11.0	1.5

Baseline. Starting with a UPT model, we train it on AhmedML ([Ashton et al., 2024a](#)) and evaluate surface pressure \mathbf{p}_s , volume velocity \mathbf{u} , and volume vorticity ω . UPT struggles with complex decoding tasks (e.g., decoding vorticity) as the decoder consists of a single cross-attention block, and hence, the vast majority of the compute is allocated to encoding.

Macro design. We make major changes to the UPT design. First, scaling the decoder to contain equally many parameters as the encoder, which greatly improves performance, at the cost of additional runtime (“+ large decoder”). As scaling the decoder greatly improved performance, we investigate a variant without any encoder by changing the decoder from cross-attending to the encoder tokens to self-attention between all query points (“+ decoder-only with self-attn”). This variant is essentially a plain transformer without any bells and whistles. While this variant improves performance further, it also loses beneficial properties and is slow in inference due to the quadratic complexity of self-attention.

Reintroducing properties. Next, we aim to modify the architecture to reintroduce beneficial properties (neural field decoder, mesh independence, and fast inference) of UPT while preserving the obtained performance gains. To this end, we introduce anchor attention (“+ anchor attention”), which converts the self-attention into a neural field by using self-attention only within a small subset of *anchor tokens*. Other tokens, the *query tokens*, only attend to the anchor tokens. This type of attention is a conditional neural field where positions

can be encoded into *query tokens*, which decodes a value for a particular position, without influencing the *anchor tokens*. This allows efficient inference as the quadratic complexity of self-attention is limited to a small number of *anchor tokens*, while creating predictions for query tokens has linear complexity due to employing cross-attention. See Section 3.2 for a detailed formulation of anchor attention.

Further, we reintroduce a light-weight geometry encoding (“+ decouple geometry encoding”) by obtaining *geometry tokens* from a light-weight UPT encoder (supernode pooling $\rightarrow 1$ transformer block, see equations 4 and 5). The first self-attention block is additionally replaced by a cross-attention to the *geometry tokens* to extract geometry information for every anchor/query token. Since the geometry encoder is not tied to any anchor/query positions, arbitrary geometry representations can be encoded. Hence, this design choice makes the model mesh independent. Additionally, this improves performance, at the cost of additional training runtime for the geometry encoder.

Micro design. Subsequently, we aim to improve speed and accuracy. For automotive CFD simulations, we aim to predict surface and volume variables where we use an equal amount of surface and volume tokens. However, these two modalities differ in the way they are calculated in a classical simulation where surface variables have boundary condition $\mathbf{u} = 0$. Therefore, we split surface and volume positions into separate branches (“+ split surface/volume branch”). This halves the number of tokens of each individual branch, resulting in faster training/inference speed and decreased performance, particularly for surface variables.

To reintroduce cross-branch interactions, we swap the keys and values of the two branches in every other block (“+ cross-branch interactions”) as visualized in Figure 4. Therefore, surface anchors/queries can retrieve information from volume anchors, and volume anchors/queries can retrieve information from surface anchors, enabling information flow between both branches at no additional cost.

Finally, we introduce branch-specific decoders by using different weights for the last L Transformer blocks (“+ branch-specific decoders”). Conceptually, this focuses on learning the physical simulation in the first K blocks (as the weights are shared between surface and volume) while additionally allocating weights/compute to branch-specific decoding.

4.4 Benchmarking AB-UPT against other neural surrogate models

Table 4: Relative L2 errors (in %) of surface pressure \mathbf{p}_s , volume velocity \mathbf{u} and volume vorticity ω . For each model, we indicate if the model has the neural field property, and whether they are mesh independent. Lower percentage values indicate better performance in terms of L2 error. We provide the results for ShapeNetCar, AhmedML, and DrivAerML. AB-UPT outperforms other neural surrogate models, often by quite a margin.

	ShapeNetCar		AhmedML			DrivAerML			Neural field	Mesh independent
	\mathbf{p}_s	\mathbf{u}	\mathbf{p}_s	\mathbf{u}	ω	\mathbf{p}_s	\mathbf{u}	ω		
PointNet	12.09	3.05	8.51	5.43	67.30	23.63	28.12	880.9	✗	✗
GRAPH U-NET	10.33	2.49	6.42	4.14	53.53	16.13	17.98	380.4	✗	✗
GINO	13.28	2.53	7.90	6.23	71.81	13.03	40.58	98.5	✓	✓
LNO	9.05	2.29	12.91	7.56	72.05	20.51	23.27	173.0	✓	✓
UPT	5.60	1.40	3.90	2.62	13.69	7.85	9.02	189.6	✓	✓
OFormer	7.05	1.61	3.55	2.21	7.78	4.48	6.64	60.4	✓	✓
Transolver	6.50	1.53	3.66	2.19	8.12	4.81	6.78	38.4	✗	✗
Transformer	5.01	1.24	3.41	2.09	6.76	4.35	6.21	47.9	✗	✗
AB-UPT	4.81	1.18	3.00	1.88	6.45	3.82	5.93	35.1	✓	✓

In this section, we compare the performance of AB-UPT against established neural-surrogate models: Table 4 presents the relative L2 error for surface pressure, volume velocity, and vorticity. We compare AB-UPT against the following models: PointNet (Qi et al., 2017a), Graph U-Net (Gao & Ji, 2019), GINO (Li et al., 2023b), LNO (Wang & Wang, 2024), UPT (Alkin et al., 2024a), OFormer (Li et al., 2023a), Transolver (Wu et al., 2024), Transformer (Vaswani et al., 2017). We do not consider Transolver++ as a baseline due to reproducibility issues, which we explain in Appendix B.4. These comparisons are conducted across

three diverse datasets: ShapeNetCar (Umetani & Bickel, 2018), AhmedML (Ashton et al., 2024a), and DrivAerML (Ashton et al., 2024b). The full experimental setup is detailed in Appendix B. Table 10 in Appendix B presents the training hyperparameters and the number of model parameters for each model. Additionally, Appendix C provides a statement on the fairness of our experimental setup in comparison to (Wu et al., 2024). Comprehensive results, including wall shear stress and volume pressure, are reported in Table 7 in Appendix A.1.

Table 4 shows that AB-UPT consistently outperforms all other neural surrogate models across every evaluated metric and dataset, often by a substantial margin. Moreover, we observe that most baselines struggle with properly modeling the complex vorticity. AB-UPT, however, maintains strong performance for both surface and volume metrics, highlighting its robustness. For most metrics, either a plain Transformer or Transolver is the second-best-performing model. However, due to the full self-attention mechanism of the Transformer, this model will not be able to scale to industry-standard simulation meshes. Transolver, on the other hand, would require sequence parallelism over multiple GPUs to handle large simulation meshes (as has been explored in (Luo et al., 2025)). We can conclude that AB-UPT is the best performing model for neural-surrogate automotive CFD simulation, while also having favorable properties concerning problem scaling.

4.5 Aerodynamic drag and lift coefficients

Accurate and fast predictions of global quantities, such as drag and lift coefficients, are crucial for designing efficient aerodynamic geometries. We evaluate the quality of the surface-level predictions of our model by computing these integrated aerodynamic quantities. Figure 6 shows prediction and reference values for drag and lift coefficients on DrivAerML. AB-UPT obtains accurate predictions as indicated by the high coefficient of determination (R^2) score. Additionally, such integrated quantities require high-resolution predictions (see Figure 1), which AB-UPT can effortlessly produce via anchor attention, despite being trained on only a small subset (e.g., 16 thousand) surface points.

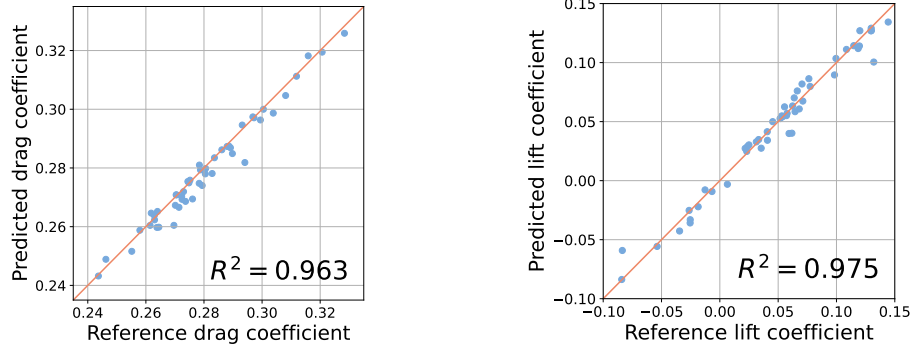


Figure 6: AB-UPT can accurately predict aerodynamic drag and lift coefficients of DrivAerML. To obtain accurate results, pressure and wall shear stress need to be predicted for millions of surface points (see Figure 1). AB-UPT can make accurate predictions for millions of surface points despite being trained with only 16 thousand surface points.

4.6 Training from CAD

A particularly intriguing property of AB-UPT is that it decouples query positions, anchor positions, and geometry encoding. This allows us to train models that can make predictions on geometry representations other than the meshed CFD geometry. To showcase this, we consider the following setting: we uniformly sample surface points from a CAD file and use these positions as inputs to the geometry encoder and as surface anchors. For volume anchors, we uniformly sample random positions in the domain. The model is then trained by using surface/volume positions from the CFD mesh as query points on which a loss is calculated. In this setting, no loss is calculated for anchor points since there is no corresponding CFD simulation results ground truth available for the anchor positions. As our model simulates physical dynamics only within

the anchor tokens (query tokens do not influence anchor tokens as they only interact via cross-attention), this enables learning an accurate neural surrogate that operates on uniform meshes. Note that a numerical simulation would either not converge or produce suboptimal results on a uniform surface/volume mesh.

Table 5 compares the accuracy of such approaches. Sampling anchor positions from the CFD simulation mesh implicitly assigns more computational resources to highly resolved regions, which typically contain complicated dynamics. Uniformly sampling from the CAD geometry removes this bias and degrades performance slightly, as expected. However, this performance degradation is fairly small, particularly when considering that numerical simulations would produce completely unusable results.

Table 5: Neural simulation without using the CFD simulation mesh on AhmedML. AB-UPT can produce accurate results even in the absence of the CFD simulation mesh, which is typically costly to obtain. Numerical simulations (e.g., HRLES) would not converge or produce unrealistic results without the CFD simulation mesh. Note that HRLES with the CFD simulation mesh is used as ground truth (i.e., 0.00 error).

	Relative L2 error (↓)			Meshing	
	\mathbf{p}_s	\mathbf{u}	ω	Surface mesh	Volume mesh
HRLES	0.00	0.00	0.00	CFD simulation mesh	CFD simulation mesh
HRLES	N.A.	N.A.	N.A.	Geometry mesh (CAD)	Regular grid
AB-UPT	3.14	2.07	6.34	CFD simulation mesh	CFD simulation mesh
AB-UPT	3.62	2.56	7.43	Geometry mesh (CAD)	Regular grid

4.7 Divergence-free vorticity

As discussed in Sections 3.2 and 3.3, the conditional field property of AB-UPT allows for defining vorticity field predictions that are divergence-free by design. We train the model in two stages: in the pretraining phase, we learn a model that predicts all surface and volume fields *except* the vorticity, using the same model configuration and hyperparameters as in the previous experiments; in the finetuning phase, we learn all fields *including* the derived vorticity field (cf. Section 3.3). Furthermore, we use float32 precision for finetuning, and we train with a smaller initial learning rate and fewer training steps: starting from $2.0 \cdot 10^{-5}$, the learning rate is decayed to $1.0 \cdot 10^{-6}$ via the cosine annealing schedule. As discussed in Section 3.3, after correcting for the scaling of the velocity field due to normalization, the predicted vorticity is already in *physics space*. To bring the predictions to a similar scale as other predicted fields, we transform both the predictions and targets as follows: first divide by the field’s standard deviation; then apply a sign-preserving square-root to the vector’s magnitude. This is equivalent to scaling the individual loss terms. All other fields are simply normalized as in all other experiments, subtracting the mean and dividing by the standard deviation (c. f. Appendix B.4.1).

Table 6 shows that the *divergence-free* vorticity formulation of AB-UPT matches the performance of the *direct-prediction* approach. However, while direct prediction results in non-zero divergence of the predicted vorticity field, the divergence-free formulation guarantees zero divergence by construction. Note that the most competitive baselines such as Transolver and Transformer do not have a (conditional) field formulation, and, thus, the local divergence operator is not defined for these models.

Table 6: Evaluation of AB-UPT with the divergence-free vorticity formulation (c. f. Section 3.3). For each dataset, the first 3 columns per datasets show the relative L2/L1 test errors (in %) of surface pressure \mathbf{p}_s , volume velocity \mathbf{u} and volume vorticity ω . The last column shows the mean absolute value of the divergence of the predicted vorticity field $\nabla \cdot \omega$ (in $m^{-1}s^{-1}$), where the average is taken over simulations and samples of the field.

	AhmedML				DrivAerML			
	\mathbf{p}_s	\mathbf{u}	ω	$\nabla \cdot \omega$	\mathbf{p}_s	\mathbf{u}	ω	$\nabla \cdot \omega$
AB-UPT (direct)	3.26/1.69	1.98/1.09	5.23/4.02	13.69	3.98/3.11	5.64/5.49	33.0/15.74	586.7
AB-UPT (divfree)	3.24/1.69	2.01/1.10	5.57/4.30	0	3.82/3.09	5.58/5.40	31.39/16.16	0

5 Limitations and future work

The bottleneck of quadratic complexity of self-attention for anchor tokens. AB-UPT employs expressive self-attention among anchor tokens, which exhibits quadratic complexity. We show that on high-fidelity CFD simulations a small set of anchor tokens is sufficient to obtain good results on currently available public datasets. However using more anchor tokens can improve accuracy further, leading to (quadratically) increasing computational demands. Contrary, the computational demands of models with linear complexity would only increase linearly.

However, we did not manage to scale linear attention models to obtain higher accuracies than AB-UPT, even when using twice the number of inputs (see Figure 5). Additionally, the trend of the loss curves in Figure 5 suggests that the benefit of scaling the number of inputs saturates. As there is still a sizable gap between the AB-UPT test loss and linear attention test loss (i.e., Transolver), it is unlikely that linear attention models would obtain better accuracies than AB-UPT, even when trained on a large number of inputs. Nevertheless, for an extremely large number of anchor tokens, compute demands would explode, and AB-UPT would need some kind of linear attention mechanisms.

Fast training through parallelization. To keep training times low, a future direction would be to apply parallelization techniques such as sequence parallelism (Liu et al., 2023) or tensor parallelism (Shoeybi et al., 2019) to scale the number of anchor tokens to the next order of magnitude. Additionally, one could easily parallelize inference by dividing the query tokens among different GPUs, which would linearly decrease inference time.

AB-UPT beyond automotive CFD. AB-UPT is a general-purpose architecture, which we expect to be applicable to many use cases beyond automotive CFD. We chose automotive CFD as a problem setting as there exist public high-fidelity datasets, which serve as a good starting point where models such as UPT and Transolver start to break as they can not model the complex dynamics of these datasets. However, as AB-UPT is a natural successor of UPT, we expect it to perform well on many simulation types, as is the case for UPT (e.g., transient fluid simulations (Alkin et al., 2024a) or particle and particle-fluid multi-physics simulations (Alkin et al., 2024b)).

6 Conclusion and outlook

In this work, we answer the question of how to define and harness scale in the context of automotive CFD simulations. We introduce Anchored-Branched Universal Physics Transformers: a neural surrogate architecture for physics simulation, which we demonstrate on high-fidelity automotive CFD simulations with up to hundreds of millions of simulation mesh cells. We investigate the notion of problem scale, where the number of mesh cells required for industry-standard numeric CFD simulation is typically correlated with the complexity of physical dynamics. However, neural surrogate models learn a conceptually different solution to the numerical equations and can simulate complex dynamics in a heavily reduced resolution. This allows us to leverage expressive self-attention to build a powerful modeling backbone. However, practical use-cases often necessitate a high-resolution prediction, e.g., to obtain accurate drag/lift coefficients. Therefore, we introduce *anchor attention*, which enables prediction at arbitrary resolution at linear complexity by leveraging a small set of *anchor tokens* as context to create predictions for arbitrary query positions.

AB-UPT outperforms strong neural surrogate benchmark models and has beneficial properties such as mesh independence, which allows neural simulation from CAD geometry alone, omitting the need for the costly creation of a CFD simulation mesh. Additionally, we make use of the neural field property of AB-UPT to formulate a divergence-free vorticity prediction to make predictions physically consistent.

References

Josh Abramson, Jonas Adler, Jack Dunger, Richard Evans, Tim Green, Alexander Pritzel, Olaf Ronneberger, Lindsay Willmore, Andrew J Ballard, Joshua Bambrick, et al. Accurate structure prediction of biomolecular interactions with AlphaFold 3. *Nature*, 630:493–500, 2024.

Jean-Baptiste Alayrac, Jeff Donahue, Pauline Luc, Antoine Miech, Iain Barr, Yana Hasson, Karel Lenc, Arthur Mensch, Katherine Millican, Malcolm Reynolds, Roman Ring, Eliza Rutherford, Serkan Cabi, Tengda Han, Zhitao Gong, Sina Samangoeei, Marianne Monteiro, Jacob L. Menick, Sebastian Borgeaud, Andy Brock, Aida Nematzadeh, Sahand Sharifzadeh, Mikolaj Binkowski, Ricardo Barreira, Oriol Vinyals, Andrew Zisserman, and Karén Simonyan. Flamingo: a visual language model for few-shot learning. In *NeurIPS*, 2022.

Giancarlo Alfonsi. Reynolds-averaged navier–stokes equations for turbulence modeling. *Applied Mechanics Reviews*, 62(4), 2009.

Benedikt Alkin, Andreas Fürst, Simon Lucas Schmid, Lukas Gruber, Markus Holzleitner, and Johannes Brandstetter. Universal physics transformers: A framework for efficiently scaling neural operators. In *NeurIPS*, 2024a.

Benedikt Alkin, Tobias Kronlachner, Samuele Papa, Stefan Pirker, Thomas Lichtenegger, and Johannes Brandstetter. NeuralDEM-real-time simulation of industrial particulate flows. *arXiv preprint arXiv:2411.09678*, 2024b.

Neil Ashton, Paul Batten, Andrew W Cary, Kevin R Holst, and Vangelis Skaperdas. HLPW-4/GMGW-3: Hybrid rans/les technology focus group workshop summary. In *AIAA Aviation 2022 Forum*, 2022.

Neil Ashton, Danielle Maddix, Samuel Gundry, and Parisa Shabestari. AhmedML: High-fidelity computational fluid dynamics dataset for incompressible, low-speed bluff body aerodynamics. *arXiv preprint arXiv:2407.20801*, 2024a.

Neil Ashton, Charles Mockett, Marian Fuchs, Louis Fliessbach, Hendrik Hetmann, Thilo Knacke, Norbert Schonwald, Vangelis Skaperdas, Grigoris Fotiadis, Astrid Walle, et al. DrivAerML: High-fidelity computational fluid dynamics dataset for road-car external aerodynamics. *arXiv preprint arXiv:2408.11969*, 2024b.

Kaifeng Bi, Lingxi Xie, Hengheng Zhang, Xin Chen, Xiaotao Gu, and Qi Tian. Accurate medium-range global weather forecasting with 3D neural networks. *Nature*, 619(7970):533–538, 2023.

Cristian Bodnar, Wessel P Bruinsma, Ana Lucic, Megan Stanley, Johannes Brandstetter, Patrick Garvan, Maik Riechert, Jonathan Weyn, Haiyu Dong, Anna Vaughan, et al. Aurora: A foundation model of the atmosphere. *Nature*, 641:1180–1187, 2025.

Steven L Brunton, Bernd R Noack, and Petros Koumoutsakos. Machine learning for fluid mechanics. *Annual review of fluid mechanics*, 52(1):477–508, 2020.

Shuhao Cao. Choose a transformer: Fourier or galerkin. In *NeurIPS*, 2021.

Angel X. Chang, Thomas A. Funkhouser, Leonidas J. Guibas, Pat Hanrahan, Qi-Xing Huang, Zimo Li, Silvio Savarese, Manolis Savva, Shuran Song, Hao Su, Jianxiong Xiao, Li Yi, and Fisher Yu. Shapenet: An information-rich 3d model repository. *arXiv preprint arXiv:1512.03012*, 2015.

Bruno Chaouat. The state of the art of hybrid RANS/LES modeling for the simulation of turbulent flows. *Flow, turbulence and combustion*, 99:279–327, 2017.

Xiangning Chen, Chen Liang, Da Huang, Esteban Real, Kaiyuan Wang, Hieu Pham, Xuanyi Dong, Thang Luong, Cho-Jui Hsieh, Yifeng Lu, and Quoc V. Le. Symbolic discovery of optimization algorithms. In *NeurIPS*, 2023.

Tri Dao, Daniel Y. Fu, Stefano Ermon, Atri Rudra, and Christopher Ré. Flashattention: Fast and memory-efficient exact attention with io-awareness. In *NeurIPS*, 2022.

Alexey Dosovitskiy, Lucas Beyer, Alexander Kolesnikov, Dirk Weissenborn, Xiaohua Zhai, Thomas Unterthiner, Mostafa Dehghani, Matthias Minderer, Georg Heigold, Sylvain Gelly, Jakob Uszkoreit, and Neil Houlsby. An image is worth 16x16 words: Transformers for image recognition at scale. In *ICLR*, 2021.

Abhimanyu Dubey, Abhinav Jauhri, Abhinav Pandey, Abhishek Kadian, Ahmad Al-Dahle, Aiesha Letman, Akhil Mathur, Alan Schelten, Amy Yang, Angela Fan, Anirudh Goyal, Anthony Hartshorn, Aobo Yang, Archi Mitra, Archie Sravankumar, Artem Korenev, Arthur Hinsvark, Arun Rao, Aston Zhang, Aurélien Rodriguez, Austen Gregerson, Ava Spataru, Baptiste Rozière, Bethany Biron, Binh Tang, Bobbie Chern, Charlotte Caucheteux, Chaya Nayak, Chloe Bi, Chris Marra, Chris McConnell, Christian Keller, Christophe Touret, Chunyang Wu, Corinne Wong, Cristian Canton Ferrer, Cyrus Nikolaidis, Damien Allonsius, Daniel Song, Danielle Pintz, Danny Livshits, David Esiobu, Dhruv Choudhary, Dhruv Mahajan, Diego Garcia-Olano, Diego Perino, Dieuwke Hupkes, Egor Lakomkin, Ehab AlBadawy, Elina Lobanova, Emily Dinan, Eric Michael Smith, Filip Radenovic, Frank Zhang, Gabriel Synnaeve, Gabrielle Lee, Georgia Lewis Anderson, Graeme Nail, Grégoire Mialon, Guan Pang, Guillem Cucurell, Hailey Nguyen, Hannah Korevaar, Hu Xu, Hugo Touvron, Iliyan Zarov, Imanol Arrieta Ibarra, Isabel M. Kloumann, Ishan Misra, Ivan Evtimov, Jade Copet, Jaewon Lee, Jan Geffert, Jana Vranes, Jason Park, Jay Mahadeokar, Jeet Shah, Jelmer van der Linde, Jennifer Billock, Jenny Hong, Jenya Lee, Jeremy Fu, Jianfeng Chi, Jianyu Huang, Jiawen Liu, Jie Wang, Jiecao Yu, Joanna Bitton, Joe Spisak, Jongsoo Park, Joseph Rocca, Joshua Johnstun, Joshua Saxe, Junteng Jia, Kalyan Vasudevan Alwala, Kartikeya Upasani, Kate Plawiak, Ke Li, Kenneth Heafield, Kevin Stone, and et al. The llama 3 herd of models. *arXiv preprint arXiv:2407.21783*, 2024.

Mohamed Elrefaie, Angela Dai, and Faez Ahmed. Drivaernet: A parametric car dataset for data-driven aerodynamic design and graph-based drag prediction. *arXiv preprint arXiv:2403.08055*, 2024a.

Mohamed Elrefaie, Florin Morar, Angela Dai, and Faez Ahmed. Drivaernet++: A large-scale multimodal car dataset with computational fluid dynamics simulations and deep learning benchmarks. In *NeurIPS*, 2024b.

Patrick Esser, Sumith Kulal, Andreas Blattmann, Rahim Entezari, Jonas Müller, Harry Saini, Yam Levi, Dominik Lorenz, Axel Sauer, Frederic Boesel, et al. Scaling rectified flow transformers for high-resolution image synthesis. In *ICML*, 2024.

Hongyang Gao and Shuiwang Ji. Graph U-Nets. In *ICML*, 2019.

Zhongkai Hao, Zhengyi Wang, Hang Su, Chengyang Ying, Yinpeng Dong, Songming Liu, Ze Cheng, Jian Song, and Jun Zhu. GNOT: A general neural operator transformer for operator learning. In *ICML*, 2023.

Stefan Heinz. A review of hybrid RANS-LES methods for turbulent flows: Concepts and applications. *Progress in Aerospace Sciences*, 2020.

Charles Hirsch. *Numerical computation of internal and external flows: The fundamentals of computational fluid dynamics*. Elsevier, 2007.

Burkhard Hupertz, Neil Lewington, Charles Mockett, Neil Ashton, and Lian Duan. Towards a standardized assessment of automotive aerodynamic CFD prediction capability-AutoCFD 2: Ford驱车器 test case summary. Technical report, SAE Technical Paper, 2022.

Andrew Jaegle, Felix Gimeno, Andy Brock, Oriol Vinyals, Andrew Zisserman, and Joao Carreira. Perceiver: General perception with iterative attention. In *ICML*, 2021.

John Jumper, Richard Evans, Alexander Pritzel, Tim Green, Michael Figurnov, Olaf Ronneberger, Kathryn Tunyasuvunakool, Russ Bates, Augustin Žídek, Anna Potapenko, et al. Highly accurate protein structure prediction with alphafold. *nature*, 596(7873):583–589, 2021.

David M Knigge, David R Wessels, Riccardo Valperga, Samuele Papa, Jan-Jakob Sonke, Efstratios Gavves, and Erik J Bekkers. Space-time continuous PDE forecasting using equivariant neural fields. *arXiv preprint arXiv:2406.06660*, 2024.

Remi Lam, Alvaro Sanchez-Gonzalez, Matthew Willson, Peter Wirnsberger, Meire Fortunato, Ferran Alet, Suman Ravuri, Timo Ewalds, Zach Eaton-Rosen, Weihua Hu, et al. Learning skillful medium-range global weather forecasting. *Science*, 382(6677):1416–1421, 2023.

Brian Edward Launder and Dudley Brian Spalding. The numerical computation of turbulent flows. *Computer Methods in Applied Mechanics and Engineering*, 3(2):269–289, 1974.

Marcel Lesieur, Olivier Métais, and Pierre Comte. *Large-eddy simulations of turbulence*. Cambridge university press, 2005.

Zijie Li, Kazem Meidani, and Amir Barati Farimani. Transformer for partial differential equations’ operator learning. *Transactions on Machine Learning Research*, 2023a.

Zijie Li, Dule Shu, and Amir Barati Farimani. Scalable transformer for PDE surrogate modeling. In *NeurIPS*, 2024.

Zongyi Li, Nikola Kovachki, Kamyar Azizzadenesheli, Burigede Liu, Kaushik Bhattacharya, Andrew Stuart, and Anima Anandkumar. Neural operator: Graph kernel network for partial differential equations. *arXiv preprint arXiv:2003.03485*, 2020.

Zongyi Li, Nikola Borislavov Kovachki, Kamyar Azizzadenesheli, Burigede Liu, Kaushik Bhattacharya, Andrew M. Stuart, and Anima Anandkumar. Fourier neural operator for parametric partial differential equations. In *ICLR*, 2021.

Zongyi Li, Nikola Borislavov Kovachki, Chris Choy, Boyi Li, Jean Kossaifi, Shourya Prakash Otta, Mohammad Amin Nabian, Maximilian Stadler, Christian Hundt, Kamyar Azizzadenesheli, et al. Geometry-informed neural operator for large-scale 3D PDEs. In *NeurIPS*, 2023b.

Hao Liu, Matei Zaharia, and Pieter Abbeel. Ring attention with blockwise transformers for near-infinite context. *arXiv preprint arXiv:2310.01889*, 2023.

Ilya Loshchilov and Frank Hutter. Decoupled weight decay regularization. In *ICLR*, 2019.

Lu Lu, Pengzhan Jin, Guofei Pang, Zhongqiang Zhang, and George Em Karniadakis. Learning nonlinear operators via DeepONet based on the universal approximation theorem of operators. *Nature machine intelligence*, 3(3):218–229, 2021a.

Lu Lu, Raphaël Pestourie, Wenjie Yao, Zhicheng Wang, Francesc Verdugo, and Steven G. Johnson. Physics-informed neural networks with hard constraints for inverse design. *SIAM Journal on Scientific Computing*, 43(6):B1105–B1132, 2021b. doi: 10.1137/21M1397908.

Huakun Luo, Haixu Wu, Hang Zhou, Lanxiang Xing, Yichen Di, Jianmin Wang, and Mingsheng Long. Transolver++: An accurate neural solver for pdes on million-scale geometries. *arXiv preprint arXiv:2502.02414*, 2025.

Amil Merchant, Simon Batzner, Samuel S Schoenholz, Muratahan Aykol, Gowoon Cheon, and Ekin Dogus Cubuk. Scaling deep learning for materials discovery. *Nature*, 624(7990):80–85, 2023.

Ben Mildenhall, Pratul P. Srinivasan, Matthew Tancik, Jonathan T. Barron, Ravi Ramamoorthi, and Ren Ng. NeRF: Representing scenes as neural radiance fields for view synthesis. In *ECCV*, 2020.

Tung Nguyen, Johannes Brandstetter, Ashish Kapoor, Jayesh K. Gupta, and Aditya Grover. ClimaX: A foundation model for weather and climate. In *ICML*, 2023.

Maxime Oquab, Timothée Darcet, Théo Moutakanni, Huy Vo, Marc Szafraniec, Vasil Khalidov, Pierre Fernandez, Daniel Haziza, Francisco Massa, Alaaeldin El-Nouby, Mahmoud Assran, Nicolas Ballas, Wojciech Galuba, Russell Howes, Po-Yao Huang, Shang-Wen Li, Ishan Misra, Michael G. Rabbat, Vasu Sharma, Gabriel Synnaeve, Hu Xu, Hervé Jégou, Julien Mairal, Patrick Labatut, Armand Joulin, and Piotr Bojanowski. Dinov2: Learning robust visual features without supervision. *arXiv preprint arXiv:2304.07193*, 2023.

Jaideep Pathak, Shashank Subramanian, Peter Harrington, Sanjeev Raja, Ashesh Chattopadhyay, Morteza Mardani, Thorsten Kurth, David Hall, Zongyi Li, Kamyar Azizzadenesheli, et al. Fourcastnet: A global data-driven high-resolution weather model using adaptive fourier neural operators. *arXiv preprint arXiv:2202.11214*, 2022.

Richard H Pletcher, John C Tannehill, and Dale Anderson. *Computational fluid mechanics and heat transfer*. CRC press, 2012.

Charles R Qi, Hao Su, Kaichun Mo, and Leonidas J Guibas. Pointnet: Deep learning on point sets for 3d classification and segmentation. In *CVPR*, 2017a.

Charles Ruizhongtai Qi, Li Yi, Hao Su, and Leonidas J Guibas. Pointnet++: Deep hierarchical feature learning on point sets in a metric space. *NeurIPS*, 2017b.

M. Raissi, P. Perdikaris, and G.E. Karniadakis. Physics-informed neural networks: A deep learning framework for solving forward and inverse problems involving nonlinear partial differential equations. *Journal of Computational Physics*, 378:686–707, 2019.

Rishikesh Ranade, Mohammad Amin Nabian, Kaustubh Tangsali, Alexey Kamenev, Oliver Hennigh, Ram Cherukuri, and Sanjay Choudhry. Domino: A decomposable multi-scale iterative neural operator for modeling large scale engineering simulations. *arXiv preprint arXiv:2501.13350*, 2025.

Osborne Reynolds. Iv. on the dynamical theory of incompressible viscous fluids and the determination of the criterion. *Philosophical transactions of the royal society of London.*, (186):123–164, 1895.

Jack Richter-Powell, Yaron Lipman, and Ricky T. Q. Chen. Neural conservation laws: A divergence-free perspective. In S. Koyejo, S. Mohamed, A. Agarwal, D. Belgrave, K. Cho, and A. Oh (eds.), *Advances in Neural Information Processing Systems*, volume 35, pp. 38075–38088. Curran Associates, Inc., 2022.

Jacob Seidman, Georgios Kissas, Paris Perdikaris, and George J Pappas. NOMAD: Nonlinear manifold decoders for operator learning. *NeurIPS*, 2022.

Louis Serrano, Thomas X Wang, Etienne Le Naour, Jean-Noël Vitta, and Patrick Gallinari. AROMA: Preserving spatial structure for latent PDE modeling with local neural fields. In *NeurIPS*, 2024.

Mohammad Shoeybi, Mostofa Patwary, Raul Puri, Patrick LeGresley, Jared Casper, and Bryan Catanaro. Megatron-lm: Training multi-billion parameter language models using model parallelism. *ArXiv*, abs/1909.08053, 2019.

Philippe R Spalart, Shur Deck, Michael L Shur, Kyle D Squires, M Kh Strelets, and Andrei Travin. A new version of detached-eddy simulation, resistant to ambiguous grid densities. *Theoretical and computational fluid dynamics*, 20, 2006.

Jianlin Su, Murtadha H. M. Ahmed, Yu Lu, Shengfeng Pan, Wen Bo, and Yunfeng Liu. RoFormer: Enhanced transformer with rotary position embedding. *Neurocomputing*, 568:127063, 2024.

Roger Temam. *Navier-Stokes equations: theory and numerical analysis*, volume 343. American Mathematical Soc., 2001.

Nils Thuerey, Philipp Holl, Maximilian Mueller, Patrick Schnell, Felix Trost, and Kiwon Um. Physics-based deep learning. *arXiv preprint arXiv:2109.05237*, 2021.

Hugo Touvron, Matthieu Cord, Matthijs Douze, Francisco Massa, Alexandre Sablayrolles, and Hervé Jégou. Training data-efficient image transformers & distillation through attention. In *ICML*, 2021.

Nobuyuki Umetani and Bernd Bickel. Learning three-dimensional flow for interactive aerodynamic design. *ACM Transactions on Graphics*, 37(4):1–10, 2018.

Ashish Vaswani, Noam Shazeer, Niki Parmar, Jakob Uszkoreit, Llion Jones, Aidan N Gomez, Łukasz Kaiser, and Illia Polosukhin. Attention is all you need. In *NeurIPS*, 2017.

H.K. Versteeg and W. Malalasekera. *An Introduction to Computational Fluid Dynamics: The Finite Volume Method*. Pearson Education Limited, 2007.

Haixin Wang, Yadi Cao, Zijie Huang, Yuxuan Liu, Peiyan Hu, Xiao Luo, Zezheng Song, Wanjia Zhao, Jilin Liu, Jinan Sun, et al. Recent advances on machine learning for computational fluid dynamics: A survey. *arXiv preprint arXiv:2408.12171*, 2024a.

Sifan Wang, Jacob H. Seidman, Shyam Sankaran, Hanwen Wang, George J. Pappas, and Paris Perdikaris. Bridging operator learning and conditioned neural fields: A unifying perspective. *arXiv preprint arXiv:2405.13998*, 2024b.

Sifan Wang, Ananyae Kumar Bhartari, Bowen Li, and Paris Perdikaris. Gradient alignment in physics-informed neural networks: A second-order optimization perspective. *ArXiv*, abs/2502.00604, 2025.

Tian Wang and Chuang Wang. Latent neural operator for solving forward and inverse PDE problems. *arXiv preprint arXiv:2406.03923*, 2024.

Yue Wang, Yongbin Sun, Ziwei Liu, Sanjay E. Sarma, Michael M. Bronstein, and Justin M. Solomon. Dynamic graph CNN for learning on point clouds. *ACM Transactions on Graphics*, 38(5):146:1–146:12, 2019.

Shizheng Wen, Arsh Kumbhat, Levi Lingsch, Sepehr Mousavi, Praveen Chandrashekhar, and Siddhartha Mishra. Geometry aware operator transformer as an efficient and accurate neural surrogate for pdes on arbitrary domains. *arXiv preprint arXiv:2505.18781*, 2025.

Haixu Wu, Huakun Luo, Haowen Wang, Jianmin Wang, and Mingsheng Long. Transolver: A fast transformer solver for pdes on general geometries. In *ICML*, 2024.

Zipeng Xiao, Zhongkai Hao, Bokai Lin, Zhijie Deng, and Hang Su. Improved operator learning by orthogonal attention. *arXiv preprint arXiv:2310.12487*, 2023.

Han Yang, Chenxi Hu, Yichi Zhou, Xixian Liu, Yu Shi, Jielan Li, Guanzhi Li, Zekun Chen, Shuizhou Chen, Claudio Zeni, et al. Mattersim: A deep learning atomistic model across elements, temperatures and pressures. *arXiv preprint arXiv:2405.04967*, 2024.

Claudio Zeni, Robert Pinsler, Daniel Zügner, Andrew Fowler, Matthew Horton, Xiang Fu, Sasha Shysheya, Jonathan Crabbé, Lixin Sun, Jake Smith, et al. A generative model for inorganic materials design. *Nature*, 639:624–632, 2025.

Xuan Zhang, Limei Wang, Jacob Helwig, Youzhi Luo, Cong Fu, Yaochen Xie, Meng Liu, Yuchao Lin, Zhao Xu, Keqiang Yan, et al. Artificial intelligence for science in quantum, atomistic, and continuum systems. *arXiv preprint arXiv:2307.08423*, 2023.

A Extended results

A.1 Full results: benchmarking AB-UPT against other neural surrogate models

Table 7: Relative L2 errors (in %) of surface pressure \mathbf{p}_s , volume velocity \mathbf{u} , volume vorticity ω , wall shear stress τ , and volume pressure \mathbf{p}_v . Lower percentage values indicate better performance in terms of L2 error. We provide the results for ShapeNetCar, AhmedML, and DrivAerML. AB-UPT outperforms other neural surrogate models, often by quite a margin. For ShapeNetCar, only surface pressure and volume velocity are available.

	ShapeNetCar				AhmedML				DrivAerML				
	\mathbf{p}_s	\mathbf{u}	\mathbf{p}_s	\mathbf{u}	ω	τ	\mathbf{p}_v	\mathbf{p}_s	\mathbf{u}	ω	τ	\mathbf{p}_v	
PointNet	12.09	3.05	8.51	5.43	67.30	10.07	6.12	23.63	28.12	880.9	41.85	31.23	
GRAPH U-NET	10.33	2.49	6.42	4.14	53.53	7.21	5.17	16.13	17.98	380.4	27.85	20.52	
GINO	13.28	2.53	7.90	6.23	71.81	8.18	8.10	3.03	40.58	98.5	21.71	44.90	
LNO	9.05	2.29	12.91	7.56	72.05	11.44	8.47	20.51	23.27	173.0	36.44	27.02	
UPT	5.60	1.40	3.90	2.62	13.69	5.52	3.01	7.85	9.02	189.6	12.70	10.54	
OFormer	7.05	1.61	3.55	2.21	7.78	4.10	2.27	4.48	6.64	60.4	8.92	7.10	
Transolver	6.50	1.53	3.66	2.19	8.12	4.00	2.16	4.81	6.78	38.4	8.95	7.74	
Transformer	5.01	1.24	3.41	2.09	6.76	4.03	2.16	4.35	6.21	47.9	8.26	6.27	
AB-UPT	4.81	1.18	3.00	1.88	6.45	3.88	1.98	3.82	5.93	35.1	7.29	6.08	

A.2 Benchmarking AB-UPT against DoMINO

Table 8: Relative L2 errors (in %) of surface pressure \mathbf{p}_s , wall shear stress τ per x, y, z , dimension, volume velocity \mathbf{u} per x, y, z dimension, and volume pressure \mathbf{p}_v . Lower percentage values indicate better performance in terms of L2 error. We provide the results for DrivAerML. AB-UPT outperforms other neural surrogate models, often by quite a margin. The results for DoMINO are taken from (Ranade et al., 2025)*.

	Surface				Volume			
	\mathbf{p}_s	τ_x	τ_y	τ_z	\mathbf{p}_v	\mathbf{u}_x	\mathbf{u}_y	\mathbf{u}_z
DoMINO*	15.05	21.24	30.2	33.59	21.93	23.97	50.25	45.67
AB-UPT	3.76	5.35	3.65	3.63	6.29	4.43	3.04	2.61

Table 8 presents a direct comparison between AB-UPT and DoMINO (Ranade et al., 2025). DoMINO is originally trained and tested using a specific data split, where 20% of the test samples are out-of-distribution, based on the range of drag force values.

We trained AB-UPT with the same train/test split as provided in (Ranade et al., 2025), and report median evaluation metrics over 5 training runs. All other hyperparameters for AB-UPT remained consistent with those reported in Appendix B. The numbers for DoMINO are taken directly from (Ranade et al., 2025) and we compare to the same metrics.

Based on Table 8, we can conclude that AB-UPT outperforms DoMINO with a sufficient margin when both models are trained and evaluated on the same data splits.

A.3 Analysis: Anchor Attention

Anchor attention updates the representation of a query token based on the anchor tokens, without influencing them. Additionally, we sample random points in space, so each query token most likely has a relatively close-by anchor token. To validate the effectiveness of anchor attention, we compare our approach against a baseline of a k-NN interpolation (Qi et al., 2017b), where we interpolate the anchor tokens after the full

forward pass to query locations via a weighted sum of the 3 nearest neighbors of each query location where the weights are based on the distance to each neighbor.

Table 9 shows that anchor attention, although only trained on a reduced resolution (e.g., trained with 16K anchor points) can produce high-fidelity predictions also for query points (e.g., up to 140 million points). It is significantly better than a simple k -NN interpolation as the model learned non-linear interactions between anchor points during training, which it can transfer “zero-shot”-like to query points, even though the query points do not influence the anchor points. This underlines the effectiveness of our approach and confirms that our model learns more sophisticated prediction schemes than linear interpolation.

Table 9: Analysis of the effectiveness of anchor attention vs a simple k -NN interpolation. Anchor attention can learn more complex interactions than a simple interpolation.

AhmedML		
	\mathbf{p}_s	\mathbf{u}
k-NN interpolation	0.00685	0.06643
Anchor-attention	0.00260	0.00684

B Experimental setup

B.1 Datasets

ShapeNet Car. The ShapeNet Car dataset, a subset of the ShapeNet dataset (Chang et al., 2015) as introduced by Umetani & Bickel (2018), specifically focuses on the car-labeled data points. Each simulation in this dataset includes a surface mesh with 3,682 points and a corresponding volume mesh with 28,504 points. Following (Alkin et al., 2024a), we remove outlier points that do not belong to the surface mesh (which results in a total of 3,586 points per surface mesh). As model input, we only consider the points on the surface mesh (i.e., without using additional signed distance function values or surface normals). Our models are then trained to predict pressure values on the surface mesh and velocity values within the volume. We adopt the same training and testing split as in Wu et al. (2024), which reserves `param0` of the dataset for testing. This results in 789 samples for training and 100 samples for testing.

AhmedML. AhmedML (Ashton et al., 2024a) is an open-source dataset that provides high-fidelity CFD simulation results for 500 geometric variations of the Ahmed car body, a widely studied bluff body in automotive aerodynamics. The dataset includes hybrid RANS-LES simulations performed using OpenFOAM, capturing essential flow physics such as pressure-induced separation and 3D vortical structures. Each mesh in the dataset contains approximately 20 million cells. Since the dataset does not provide a predefined split for training, validation, and testing, we randomly divide the data into 400 train, 50 validation, and 50 test samples. Our models are then trained to predict pressure values and wall shear stress on the surface mesh and velocity, pressure, and vorticity values within the volume.

DrivAerML. The DrivAerML (Ashton et al., 2024b) dataset is designed for machine learning for high-fidelity automotive aerodynamic simulation. The dataset contains 500 parametrically morphed variants of DrivAer vehicles, aiming to address the challenge of the availability of open-source data for large-scale (in terms of the size of the simulation mesh) computational fluid dynamics (CFD) simulations in automotive aerodynamics. DrivAerML runs the CFD simulations on approximately 140 million volumetric mesh grids with Hybrid RANS-LES (Spalart et al., 2006; Chaouat, 2017; Heinz, 2020; Ashton et al., 2022), which is the highest-fidelity CFD approach used by the automotive industry (Hupertz et al., 2022; Ashton et al., 2024b). Each mesh in the dataset contains approximately 8.8 million surface points, with pressure and wall shear stress values on the surface and velocity, pressure, and vorticity values in the volume. When computing the drag and lift coefficient with AB-UPT, all 8.8 million points on the surface mesh are used. Since the dataset does not provide a predefined split for training, validation, and testing, we randomly divide the data into 400 train, 50 validation 34 validation (minus the 16 hidden samples), and 50 test samples. The dataset does not contain

results for 16 DrivAer vehicles, which we assign to the validation set, resulting in 34 effective validation samples.

B.2 Evaluation metrics

In this work, we mainly report the relative L2 error. The relative L2 error between a predicted vector of a point cloud $\hat{\mathbf{Y}} \in \mathbb{R}^{N \times d_{out}}$ and its ground truth counterpart $\mathbf{Y} \in \mathbb{R}^{N \times d_{out}}$, where N is the number of points and d_{out} is the dimensionality of the target output vector, is defined as

$$L2_{\text{rel}}(\mathbf{Y}, \hat{\mathbf{Y}}) = \frac{\|\hat{\mathbf{Y}} - \mathbf{Y}\|_2}{\|\mathbf{Y}\|_2} = \frac{\sqrt{\sum_{n=1}^N \sum_{d=1}^{d_{out}} (\hat{\mathbf{Y}}_{n,d} - \mathbf{Y}_{n,d})^2}}{\sqrt{\sum_{n=1}^N \sum_{d=1}^{d_{out}} \mathbf{Y}_{n,d}^2}}.$$

Our dataset consists of a set of M target vectors in point clouds $\mathcal{Y} = \{\mathbf{Y}^{(1)}, \mathbf{Y}^{(2)}, \dots, \mathbf{Y}^{(M)}\}$ and corresponding predictions $\hat{\mathcal{Y}} = \{\hat{\mathbf{Y}}^{(1)}, \hat{\mathbf{Y}}^{(2)}, \dots, \hat{\mathbf{Y}}^{(M)}\}$ where the average relative L2 error is defined as:

$$L2_{\text{rel}}(\mathcal{Y}, \hat{\mathcal{Y}}) = \frac{1}{M} \sum_{m=1}^M L2_{\text{rel}}(\mathcal{Y}^{(m)}, \hat{\mathcal{Y}}^{(m)}).$$

During training, the target values are normalized to approximately mean 0 and standard deviation 1, where we additionally apply a log scaling to the vorticity values. The evaluation metrics are computed on the unnormalized targets and predictions.

B.3 AB-UPT

In the following subsection, we use the a/b/c notation to indicate hyperparameters for ShapeNet-Car/AhmedML/DrivAerML, respectively. We use a radius of 9/0.25/0.25 for the supernode pooling in the geometry branch. The geometry branch consists of a supernode pooling layer, followed by a single transformer block with self-attention. The number of supernodes in the geometry branch is 3586/16384/16384, which we also use as the number of surface anchor points in the surface branch. The number of volume anchor points is 4096/16384/16384. When comparing against baselines, we train without any query tokens, i.e., we create predictions for each anchor token and calculate the loss those. In other settings (e.g., when training with the CAD geometry), we also use query tokens during training, where we set the number of query tokens to be equal to the number of anchor tokens.

We choose the architecture such that surface/volume tokens traverse 12 transformer blocks. The first block in each branch is a cross-attention block to the output of the geometry branch. The next 8/8/4 blocks consist of interleaved cross-attention and self-attention blocks, where cross-attention blocks exchange information between branches by using tokens of the other branch as keys and values. The self-attention blocks operate only within their branch. The last 3/3/7 blocks are also self-attention blocks. Afterwards, a linear layer decodes the token representation into 4 surface variables (1 pressure dimension, 3 wallshearstress dimensions) and 7 volume variables (1 pressure dimension, 3 velocity dimension, 3 wallshearstress dimensions).

We use a standard ViT (Dosovitskiy et al., 2021)-style pre-norm transformer blocks where we additionally add Rotary Position Embeddings (RoPE) (Su et al., 2024) to all blocks.

We train models for 500 epochs using batch size 1, LION optimizer (Chen et al., 2023) with peak learning rate 5e-5, weight decay 5e-2, a linear warmup for 5% of the training duration, followed by cosine decay with end learning rate of 1e-6. We train in float16 mixed precision and employ a mean squared error. Training takes roughly 3/7/7 hours on a single NVIDIA H100 GPU and occupies 4GB of GPU memory. Similar to (Wu et al., 2024), we choose batch size 1 because it obtains the best accuracy.

B.4 Baseline models

GINO. The Geometry Informed Neural Operator (GINO) (Li et al., 2023b) is a neural operator with a regularly structured latent space that learns a solution operator of large-scale partial differential equations.

It exhibits, as AB-UPT, a decoupling of its geometry encoder and the field-based decoder. To allow for an efficient application of the Fourier Neural Operator (FNO) (Li et al., 2021), GINO transforms an irregular grid into a regular latent grid. In particular, it starts with employing a Graph Neural Operator (GNO) to map the irregular point cloud input to a regularly structured cubic latent grid. This structured latent space is then processed by the FNO. As a last stage, a second GNO block is employed as a field decoder to get query-point-based predictions in the original irregular point cloud space (e.g., on the surface manifold of a car geometry). To ensure a fair comparison with other baselines, all of which rely solely on the point cloud geometry, we also remove the SDF input feature for GINO. For our GINO implementation (similar to the one in (Alkin et al., 2024a)), we use a latent resolution of 64^3 , 16 Fourier modes, and a message passing radius of 10. For GINO, we train two models: one for surface and one for volume predictions. GINO maps both the surface and volume mesh to a regular grid. However, the volume mesh is much larger than the surface mesh, and hence, the geometry of the car is only represented by a small fraction of the entire regular grid, which leads to a degradation of the surface predictions.

Graph U-Net. Graph U-Net (Gao & Ji, 2019) is a specialized U-net network architecture designed for irregular grids, specifically graphs. To enable the U-Net architecture to work effectively with irregular graph structures, the Graph U-Net introduces two critical operations: a Graph Pooling layer that acts as the downsampling mechanism and a Graph Unpooling layer that restores the graph to a larger size. These two components allow the Graph U-Net to maintain the U-shaped encoder-decoder structure and skip connections. We use the public implementation from the Neural-Solver-Library (Wu et al., 2024).³ To construct the neighborhood structure of the graph, we use K-nearest-neighbors, with $k = 20$.

LNO. The Latent Neural Operator (LNO) is a transformer-based neural operator that operates in a low-dimensional latent space, rather than the high-dimensional input/geometry space. LNO consists of an embedding layer that maps the raw input features/function to high-dimensional latent representations. A physics-cross-attention block that maps the input embedding to a low-dimensional number of latent tokens. Followed by several Transformer blocks that process these latent tokens. Finally, a decoder that maps the processed latent tokens back to the input space, predicting the PDE solution. We use the standard ViT-tiny configuration with 12 Transformer blocks, a channel size of 192, 3 self-attention heads, and an up-projection ratio of 4. Our implementation is based on (Wang & Wang, 2024), but adapted for the 3D aerodynamics.⁴

PointNet. PointNet (Qi et al., 2017a) is a point-based baseline model that processes the input point cloud at both local and global levels. Each point in the input point cloud is first mapped through an MLP. Next, a max-pooling operation is applied to these point features to obtain a global feature representation that captures the structure of the entire point cloud. Then, each point feature vector is concatenated with the global feature vector to give global context to each point representation. Finally, the combined representation is mapped through another MLP to predict the output signal for each point on the input surface mesh. We use the public implementation from the Neural-Solver-Library (Wu et al., 2024), where we tune n_{hidden} per dataset.⁵

OFormer. The OFormer (Li et al., 2023a) is a transformer-based encoder-decoder architecture which leverages linear attention mechanism (Cao, 2021) to deal with high-dimensional problems/functions. The raw input features are first embedded with RoPE positional information into tokens. Next, several Transformer blocks are applied. Finally, a decoder (i.e., cross-attention + MLP) maps output queries into the PDE solution. Our implementation is based on (Li et al., 2023a), but adapted for the 3D aerodynamics.⁶ For our implementation, we use Galerkin attention. We use the standard ViT-tiny configuration with 12 Transformer blocks, a channel size of 192, 3 self-attention heads, and an up-projection ratio of 4.

Transolver. Transolver (Wu et al., 2024) is a transformer-based baseline model and, at the time of writing, the state-of-the-art on ShapeNet Car. It introduces the Physics-Attention mechanism, where each layer in the Transolver model takes a finite discrete point cloud representation of an input geometry as input, and maps each point to a learnable slice (also referred to as physics tokens). Points with similar physical properties are mapped to the same slice. First, each surface mesh point is mapped to slice weights, which indicate the

³https://github.com/thuml/Neural-Solver-Library/blob/main/models/Graph_UNet.py

⁴<https://github.com/L-I-M-I-T/LatentNeuralOperator/blob/main/LNO-PyTorch/ForwardProblem/module/module.py>

⁵<https://github.com/thuml/Neural-Solver-Library/blob/main/models/PointNet.py>

⁶<https://github.com/BaratiLab/OFormer>

degree to which each point belongs to a slice. Next, the slice weights are used to aggregate point features into physics-aware tokens. Multi-head self-attention is applied to these physics-aware tokens, rather than directly to the input points, which reduces the computational cost of the self-attention layer. Finally, after the self-attention layer, the physics-aware tokens are transformed back to mesh input points by deslicing. Afterward, a feed-forward layer is applied to the individual input point representations.

We reimplement Transolver according to the official implementation of (Wu et al., 2024)⁷ and using a standard ViT-tiny configuration with 12 Transolver blocks, a channel size of 192, 3 self-attention heads, and an up-projection ratio of 4 for the feed-forward layers.. We use 512 slices in the Transolver attention, which we chose after varying the number of slices, where we did not obtain significant improvements for larger numbers of slices.

Transolver++. As Transolver++ (Luo et al., 2025) has no publicly available implementation, we attempted to reimplement it to the best of our abilities and tried to infer implementation details that are not outlined in the paper. However, contrary to the results of the original paper, our reimplementation performed consistently worse than the vanilla Transolver (Wu et al., 2024). Therefore, we do not consider it in the experiments section.

UPT. The Universal Physics Transformer (UPT) (Alkin et al., 2024a) is a unified neural operator without a grid- or particle-based latent structure, that can be applied to a variety of spatio-temporal problems. Similar to GINO (Li et al., 2023b), UPT allows for querying the latent space at any point in the spatial-temporal domain. The input function, which is represented as a point cloud, is first mapped to a lower-dimensional (in terms of the number of input tokens) representation by a (message passing) supernode pooling layer. Next, a transformer-based encoder stack maps the supernode representations into a compressed latent representation. We do not use perceiver pooling as the increased compute efficiency of further compressing the input comes at the cost of accuracy, where we value accuracy over efficiency in our work. To query the latent space at any location, cross-attention blocks are used. To give approximately equal compute to all baseline models, we use 12 cross-attention blocks instead of 1.

B.4.1 Data pre-processing

Input coordinates. For most baselines, the input coordinates are normalized with the mean and standard deviation of the input domain of the train set. For AB-UPT, GINO, OFormer, and UPT, however, scale the input coordinates within a range of [0, 1000].

Output targets. The surface/volume, velocity, and vorticity are all normalized with mean and standard deviation. Next to that, we use a log-scale for the vorticity.

Input size.. For Shapenet, we train our models with 3586 points from the surface mesh and 4096 points in the volume. For both AhmedML and DrivAerML, we train our models with 16384 surface and volume points. To make the comparison with baseline models possible in Section 4.4, we chunk the evaluation meshes into chunks of 16384 for both the surface and volume.

B.5 Training details

B.5.1 General configurations

For each baseline model, we used the AdamW (Loshchilov & Hutter, 2019) optimizer, with the exception of AB-UPT/UPT/Transformer, where we use LION (Chen et al., 2023). We tuned the learning rate of models trained with AdamW by sweeping over $\{1e-3, 5e-3, 2e-3, 5e-3, 1e-4, 5e-5, 2e-5\}$ to achieve optimal performance per baseline. Whenever LION is used, we use $5e-5$ as this value has performed consistently well. Training was conducted using either float16 or bfloat16 precision, depending on which yielded the best results. An exception was made for GINO, as it exhibited unstable behavior with float16/bfloat16 mixed precision. All models were trained for 500 epochs with a batch size of 1. We applied a weight decay of 0.05 and a gradient clipping value of 1. A cosine learning rate schedule was implemented, including a 5% warm-up phase and a final learning rate of $1.0e-6$

⁷<https://github.com/thuml/Transolver/blob/main/Car-Design-ShapeNetCar/models/Transolver.py>

For all Transformer-based models, we use the ViT-tiny configuration (Touvron et al., 2021). I.e., 12 blocks, 3 attention heads, and a hidden dimensionality of 192. This is to make sure that all our Transformer-based models are in the same range of trainable parameters.

B.5.2 Model specific hyper-parameters

Per model, we tuned some model-specific details:

PointNet. We tuned the expansion factor of the hidden dimensionality in a range of $\{16, 32, 64, 128\}$.

LNO. For LNO, we tuned the number of latent modes (i.e., the number of latent tokens) in a range of $\{128, 256, 512, 1024, 2056\}$.

Graph-UNet. To create the graph structure of the input meshes, we use k-nearest-neighbors with $k = 20$. We use an n_{hidden} of 128.

GINO. For GINO, we use a grid size of 64, a max number of input neighbors of 10, and a radius graph of 5.

UPT. We use the same settings as for AB-UPT for radius (9 for ShapeNet-Car, 0.25 for AhmedML/DrivAerML) and number of supernodes (3586 for ShapeNet-Car, 16384 for AhmedML/DrivAerML).

Table 10: Training hyper-parameters and the number of trainable parameters for each model. Where a parameter varies across datasets, it’s presented in the format ShapeNetCar, AhmedML, DrivAerML; otherwise, a single value applies to all.

Model	LR	Precision	Model specific hyper-params	Model Params
PointNet	$\{1e^{-3}, 5e^{-4}, 5e^{-4}\}$	float16	64	3.6M
GRAPH U-NET	$1e^{-3}$	{float16, bfloat16, float16}	-	14.11M
GINO	$\{1e^{-4}, 2e^{-4}, 5e^{-4}\}$	float32	-	15.6M
LNO	$\{5e^{-4}, 2e^{-4}, 1e^{-3}\}$	{bfloat16, float16, bfloat16}	$\{2056, 256, 1024\}$	6.3M
UPT	$5e^{-5}$	float16	$\{3586, 16384, 16384\}$	10.98M
OFormer	$\{2e^{-4}, 2e^{-4}, 1e^{-3}\}$	bfloat16	-	6.1M
Transolver	$1e^{-3}$	bfloat16	-	5.49M
Transformer	$5e^{-5}$	float16	-	5.49M
AB-UPT	$5e^{-5}$	float16	-	{6.71M, 8.75M, 8.75M}

B.5.3 Evaluation variance reduction

When evaluating against baseline models (including AB-UPT), we use the following protocol:

- (i) each model is trained 5 times with different random seeds, where the final result is the median of the 5 models;
- (ii) the final model weights of each run are an exponential moving average (EMA) of model weights from previous updates (EMA update factor = 0.9999);
- (iii) each test sample is divided into chunks to match the number of inputs used during training, where the number of volume cells is first subsampled to match the number of surface cells.
- (iv) evaluation results are averaged over 10 evaluation runs (i.e., we run 10 times over the entire evaluation set).

These precautions aim to facilitate a fair comparison against baseline models, as we observed a high variance in experimental results due to the small number of train/test samples and optimal results being obtained when using a batch size of 1.

Motivation. (i) reduces the impact of model initialization, dataset shuffling, and point sampling. (ii) averages gradient noise from the low batch size, since we train with a batch size of 1 similar to (Wu et al., 2024). (iii) is motivated by the fact that baseline models without a neural field decoder would require complicated multi-GPU and multi-node inference pipelines to evaluate million-scale meshes (e.g., AhmedML and DrivAerML). Additionally, using more inputs during testing than during training creates a train-test

discrepancy, leading to performance drops if models are not designed for that. (iv) aims to smooth out noise from the stochastic evaluation process; stochasticity is induced via (iii) and model-specific stochastic processes, such as choosing anchor tokens. For (i), we report the median model performance over different seeds to compensate for performance outliers.

Note that this protocol was designed with limitations of baseline models in mind. AB-UPT can decode meshes of any size on a single GPU, train with batch size > 1 on a single GPU (i.e., memory constraints are not the reason why we train with batch size 1), and decode more inputs during inference than in training.

C Baseline fairness and reproducibility

Table 11: Comparison of our baseline model evaluated on ShapeNetCar, run in the same experimental set-up as in the Transolver paper. Evaluating median and best performance over 5 training runs with different seeds for \mathbf{p}_s and \mathbf{u} , alongside the results reported in the Transolver paper. The results for AB-UPT are from Table 4 (*).

Model	Median		Best		Transolver paper	
	\mathbf{p}_s	\mathbf{u}	\mathbf{p}_s	\mathbf{u}	\mathbf{p}_s	\mathbf{u}
PointNet	12.33	4.51	10.84	3.56	11.04	4.94
GRAPH U-NET	9.87	3.97	9.66	3.88	11.02	4.71
GINO	9.32	2.69	9.21	2.64	8.10	3.83
LNO	7.71	2.26	7.51	2.14	-	-
UPT	8.77	2.20	6.90	2.00	-	-
OFormer	6.58	1.70	6.52	1.66	-	-
Transolver	7.21	2.00	6.97	1.90	7.45	2.07
Transformer	5.75	1.51	5.61	1.34	-	-
AB-UPT*	4.81	1.18	-	-	-	-

In this work, we train and evaluate AB-UPT and all the baseline models in our unified experimental framework. Some of our baselines are taken from the Neural-Solver-Library (Wu et al., 2024). To validate the correctness of our experimental framework and baseline implementations, we rerun all the ShapeNetCar experiments with the experimental setup as reported in Wu et al. (2024) (including the same input features: SDF and normal vectors in our own framework. We report the median/best pressure (\mathbf{p}_s) and velocity (\mathbf{u}) values over five training runs with different seeds, and where possible, we compare the values with the evaluation metrics reported in Wu et al. (2024). For each Transformer-based model, we use 8 Transformer blocks, with 8 attention heads, and a hidden dimensionality of 256, similar to Transolver.

As shown in Table 11, our best-performing models either match or surpass the reported results from the Transolver paper. Notably, the median results for the Transolver baseline are especially close to those reported in the original publication. Our AB-UPT model (median results from Table 4, without the additional SDF and normal vectors) still outperforms all baselines with a sufficient margin. All other baselines not reported in the Transolver paper performed as anticipated. The goal of these experiments is not to achieve better (baseline) performance but to validate the fairness and correctness of our experimental setup. Based on these results, we conclude that our experimental framework is robust and fair when compared to the work by Wu et al. (2024). Any differences observed with the values in Table 4 are attributable to consistently applied changes for all models within our experimental setup. While our results in general align with those reported in Wu et al. (2024), slight variations are still there due to randomness in model training and unavoidable minor implementation differences.